République Algérienne Démocratique & Populaire

Ministère de l'Enseignement Supérieur et de la Recherche Scientifique

Université Ziane Achour – Djelfa
Faculté des Sciences et de la Technologie
Département des Sciences de la Matière

MSIL Materials Science and Informatics Laboratory

First Principles Investgation of Structural, Optoelectronic and Elastic Properties of $Mg_{1-x}Fe_xO$

BY

Naima FAKROUN

A Dissertation submitted to the Materials Science and Informatics Laboratory in partial fulfillment of the requirements for the Degree of

Master of Physics

Speciality : Materials Physics

“ First Principles Investgation of Structural, Optoelectronic and Elastic Properties of $Mg_{1-x}Fe_xO$," a dissertation prepared by N. Fakroun in partial fulfillment of the requirements for the degree, Master of Physics , has been approved and accepted by the following:

Ahmed Gueddim

Advisor

Abdellah Kouzou

Advisor Chairman of the Examining Committee

Committe in charge

Pr. Nadir Bourissa, *University of M'sila, Examiner*

Dr. Abdelkrim Naas, *University of Djelfa, Examiner*

DEDICATION

I dedicate my dissertation work to my family and many friends. A special feeling of gratitude to my oving parents, whose words of encouragement and push for tenacity ring in my ears. I also dedicate this dissertation to my many friends who have supported me throughout the process.

ACKNOWLEDGMENTS

I wish to thank my committee members who were more than generous with their expertise and precious time. A special thanks to Dr. Ahmed Gueddim, my advisor for his countless hours of reflecting, reading, encouraging, and most of all patience throughout the entire process. Thank you Pr. Nadir Bourissa, Dr. Abdellah Kouzou, Dr. Abdelkrim Naas for agreeing to serve on my committee.

CONTENTS

LIST OF TABLES

LIST OF FIGURES

Introduction

Ferropericlasse $Mg_{1-x}Fe_xO$ is the second most abundant mineral of the lower mantle, formed by the dissociation of (Mg,Fe)SiO_3 (perovskite) and (Mg,Fe)O (ferropericlase). MgO shows no phase transitions up to at least 227 GPa [1], which is also confirmed by ab initio simulations [2].

FeO wüstite undergoes a number of pressure-induced transitions. First, there is a structural transition from the cubic to a trigonally distorted structure [3], and the transition pressure strongly depends on the hydrostaticity [4], and probably also on the NaCl-related structure to an NiAs-like hexagonal structure [5] . There are also several pressure-induced electronic transformations in FeO: antiferromagnetic ordering at about 5.5 Gpa [6,7] and a possible high to low-spin transformation at approximately 100 GPa [8], although this transition was not confirmed by X-ray emission study [9].

Structural phase transitions are not expected to occur in low-Fe containing ferropericlase. MgO is the dominant component in lower mantle ferropericlasse, and it is extremely stable in the NaCl-like B1 structure. The minimum iron content for which a trigonal distortion has been observed in magnesiowüstites under high pressure is more than 50 mole % [10-12]. Transformation to the B8 structure is even less probable for low-iron ferropericlase. Magnetic ordering also requires a significant iron concentration in order to propagate long-range spin orientation throughout the entire crystal. In addition, high temperature in the Earth's mantle should suppress any possible magnetic ordering. A spin-pairing transition, however, does not require a high iron concentration and could occur in iron-bearing minerals under high-pressure conditions in the lower mantle. An iron spin-pairing transition in the mantle was first predicted more than 40 years ago [13]. The effective radius of the high-spin electronic state is generally smaller than that of the low-spin state, and the pressure-induced bond length reduction and phase transitions to dense polymorphs would stabilize the low-spin state of Fe^{2+}. Pressure also increases crystal field splitting and, at the same time, the covalence of the chemical bonding (The Racah parameter B decreases), and all these changes would also shift the thermodynamic equilibrium to the low-spin configuration [14].

There are several possible consequences of a spin transition in the mantle. The first and the most trivial is the loss of magnetism. For Fe^{2+} there are four unpaired electrons in the high-spin state, and no unpaired electrons in the low-spin state. Differences in macroscopic properties between paramagnetic and diamagnetic states are not so important for geophysics. The second and much more i mportant for geophysics. The second and much more important is the possible change in density and compressibility due to a spin-pairing transition. Such a change would be of great importance for Earth modeling, because it would directly affect the seismological profile.

Third, a pressure induced contraction of interatomic distances could lead to an enrichment of low-spin Fe^{2+} ions of host phases in the mantle. If two compounds contain cations of the same charge, the one with the larger cation generally has the lower melting point. At low pressures, the Fe end members of ferromagnesian silicate solid solution series have lower melting points than the Mg end-members, with the result that crystallization leads to enrichment of Mg in the mineral and Fe in the liquid. At pressures above the spin-pairing transition point, however, low-spin Fe2+ may have a smaller ionic radius than Mg^{2+}, and could possibly lead to a reversal of melting point relationships [14]. The same effect could also result in significant changes of the partitioning of iron between the main iron –bearing phases, namely ferropericlase and Mg-Si perovskite [15]. Finally, a spin-pairing transition would also shift absorption bands in minerals due to changes in the electronic configuration. Since the main mechanism of thermal transport in the mantle is radiation, a spin transition could also significantly affect thermal transport properties of the mantle [16].

This study is generally focused on the structural, electronic, optical and elastic properties of MgFeO in the rock salt phase. The investigations are performed using density functional theory with several formulations as for the exchange-correlation. The manuscript is organized as follows:

In chapter 1 we present an overview of the fundamental physical properties of MgFeO. The calculation theory frame work is addressed in chapter 2. Finally the most important outcoming results are summarized and discussed in chapter 3.

BIBLIOGRAPHY

[1] T.S. Duffy, R.J.Hemley, H.K.Mao, Phys.Rev.Lett 74, (1995)1371.

[2] A.R. Oganov, M.J. Gillan, G.D. Price Ab initio lattice dynamics and structural stability of MgO. Jour.Chem.Phys 118, 10174-10182 (2003).

[3] G. Zou, H.K. Mao, P.M. Bell and D. Virgo High-pressure experiments on the iron oxide wüstite (Fe1-xO). Carnegie Institution of Washington Yearbook 79, 374-376(1980).

[4] L. Dubrovinsky, N. Dubrovinskaia,S. Saxena, T. LiBehan (2000-II) X-ray diffraction under non-hydrostatic conditions in experiments with diamond anvil cell: wustite (FeO) as an example. Material Sciences and Engineering A 288, 187-190.

[5] Y. Fei and H.K. Mao. In situ determination of the NiAs phase of FeO at high pressure and temperature. Scie 266, 1678-1680 (1994).

[6] I.Yu.Kantor, L.S. Dubrovinsky, C.A. McCammon (2005-II) Mössbauer spectroscopy at elevated pressures and temperatures: Spin transition in (Mg0.8Fe0.2)O ferropericlase.

[7] S. Nasu. High pressure Mössbauer spectroscopy using a diamond anvil cell. Hyperfine Interactions 90, 59-75(1994).

[8] M.P. Pasternak, R.D. Taylor, R. Jeanloz, X. Li, J.H.Nguyen, and C.A. McCammon High Pressure Collapse of Magnetism in Fe0.94O: Mössbauer Spectroscopy Beyond 100 GPa. Phys.Revi.Lett 79, 5046-5049(1997).

[9] J. Badro, V.V. Struzhkin, J. Shu, R.J. Hemley, H.K.Mao, C.C. Kao, J.P. Rueff, G. Shen. Magnetism in FeO at Megabar Pressures from X-Ray Emission Spectroscopy. Phys.Revi.Lett 83, 4101-4104(1999).

[10] W. Mao, J. Shu, J. Hu, R. Hemley, and H.K. Mao Displacive transition in magnesiowustite. Jour.Phys: Cond. Matt 14, 11349-11354(2002).

[11] T. Kondo, T. Ohtanix, T. Yagi, T. Kikegawa In-situ X-ray Study of (Mg,Fe)O Under High Pressure and Temperature. Journal of Conference Abstracts 7, 57(2002).

[12] T. Kondo, E. Ohtani, N. Hirao, T. Yagi, and T. Kikegawa Phase transitions of (Mg,Fe)O at megabar pressures. Phys.Eart. Plan. Inte 201, 143-144(2004).

[13] W.S. Fyfe. The possibility of d-electron coupling in olivine at high pressures. Geochemical et Cosmochimical Acta 19, 141-143(1960).

[14] R.G. Burns. Mineralogical Applications of Crystal Field Theory (second edition).Cambridge University Press, (1993).

[15] J. Badro, G. Fiquet, F. Guyot, J.P. Rueff, V.V. Struzhkin, G. Vankó, and G. Monaco Iron partitioning in Earth's mantle: Toward a deep lower mantle discontinuity. Science 300,789-791(2003).

[16] A.F. Goncharov, V.V. Struzhkin, and S.D. Jacobsen Reduced radiative conductivity of low-spin (Mg,Fe)O in the lower mantle. Science 312, 1205–1208(2005).

CHAPTER 1

PERICLASE, WUSTITE AND MIXTURE IN LOWER MANTLE

1.1 Introduction

The oxide MgO is one of the simplest binary compounds known. At ambient conditions MgO is isostructural with NaCl, which consists of cubic packing of oxygen ions and produces cubic and octahedral crystals. There are no polymorphs of MgO known to exist from experimental work, both at high- or low-temperatures and at high pressures up to at least 227 GPa [1]. MgO is believed to be mainly an ionic crystal, and there are many examples of ionic crystals with the NaCl (B1) structure which transform at high pressure into the CsCl (B2) structure. From theoretical calculations, this transition in MgO is expected at very high pressures, not yet accessed by experiments. The main controversy between different calculations has been the exact value of the transition pressure, with estimates ranging from 200 to over 1000 GPa. Calculations with the most accurate approximations give transition pressures of ~510 GPa [2,3]. MgO is one of the best studied materials. Its vibrational and elastic properties have been precisely measured experimentally [4] and also well reproduced by ab initio calculations [3]. MgO is also often used as an internal pressure marker in high-pressure experiments [5-7].

FeO has a more complicated crystal chemistry compared to MgO. In many ways this “simple” binary compound remains enigmatic even after several decades of intense experimental and theoretical studies [8]. If an ideal sample of stoichiometric wüstite,

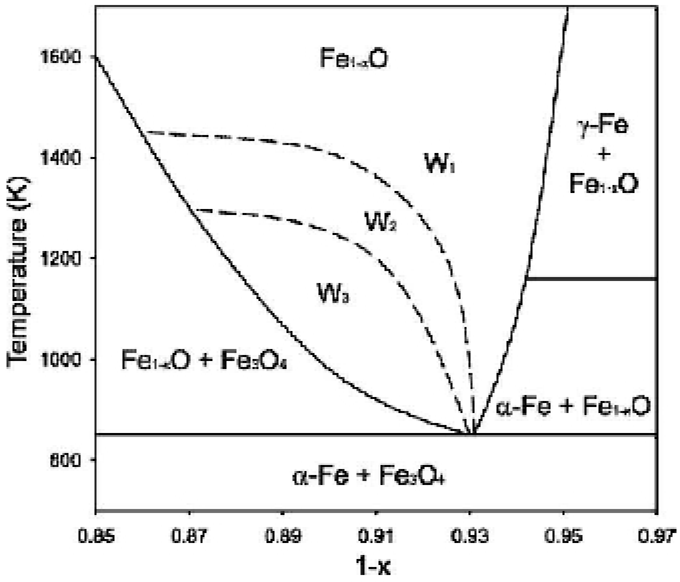

Figure 1.1: The temperature-composition phase diagram for $\mathrm{Fe}_{1-x}\mathrm{O}$. W1, W2 and W3 are hypothetical phases of $\mathrm{Fe}_{1-x}\mathrm{O}$ where these subdivisions are based on thermochemical properties .

FeO, could be prepared at ambient pressure, it would presumably have the rocksalt B1 structure similar to MgO. However, at ambient pressure and temperature ideal FeO is unstable, presumably because Fe^{2+} can be very easily oxidized to Fe^{3+}. FeO synthesized at ambient pressures never has a stoichiometric composition, but always a certain iron deficit is observed, and its chemical formula is written as $Fe_{1-x}O$. $Fe_{1-x}O$ is a typical example of a non-stoïchiometric compound with variable composition.

The phase diagram of $Fe_{1-x}O$ has been studied for many years and has undergone various revisions which always seem to reveal more complexities [9]. A simplified compositional phase diagram of the $Fe^{-}O$ system in the $Fe_{1-x}O$ region is shown in figure 1.1

From Figure 1.1 it is immediately seen that below 840 K $Fe_{1-x}O$ is not stable and decomposes into metallic iron and Fe_3O_4 magnetite. At high temperatures $Fe_{1-x}O$ is stable over a relatively broad compositional range. Figure 1.1 indicates the presence of three subdivisions of the $Fe_{1-x}O$ phase as proposed by several authors [10] on the basis of equilibrium high-temperature studies. However, this subdivision was not confirmed by other studies [11]. The difference in thermochemical properties between the W1, W2 and W3 phases could be attributed to different defect structures in $\mathrm{Fe}_{1-x}\mathrm{O}$.

Introducing an interstitial Fe^{3+} ion results in a strong local charge misbalance, and to compensate for it, the four nearest iron octahedral positions become vacancies. Thus, a 4:1 [12] cluster (the 4:1 notation is used to show 4 vacancies and 1 interstitial) can be formed (Figure 1.2.a). It is the 4:1 cluster that is believed to be the main building block for various possible defect clusters in FeO.

A large range of different defect clusters can be constructed from the 4:1 building block. For example, three edge-sharing clusters could form a 8:3 chain (Figure 1.2.b), and so on.Different defect clusters can be characterized by the vacancy to interstitial ratio ρ, which usually varies between 2.7 and 3. The minimum possible value for ρ is 1.5 (full charge compensation of interstitials and vacancies). Some measurements suggest ρ to have a value as high as 3.2, which is compatible with the proposed 13:4 cluster [13] (Figure 1.2.c). Different defect clusters could exist in the FeO structure, and cluster geometry also varies with the composition and, perhaps, temperature. The defect structure of FeO is further complicated by relative arrangement of defect clusters in the crystal structure. Based on the analysis of diffuse scattering around incommensurate diffraction peaks, it was shown that the defect cluster distribution is not random, and

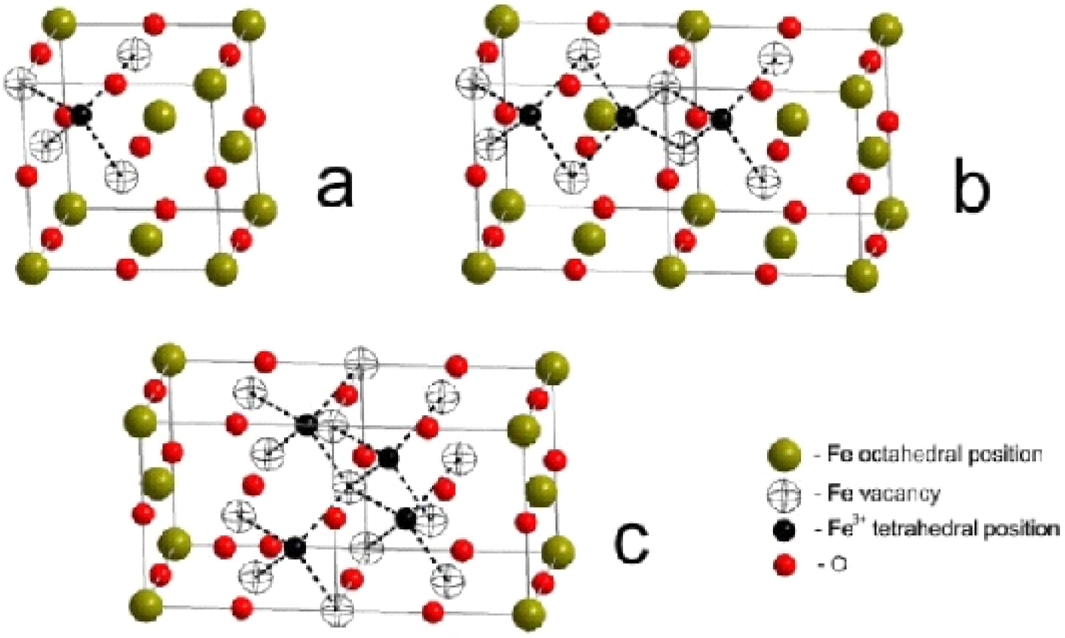

Figure 1.2: Defect clustering in FeO. a – elementary 4:1 cluster, b – 8:3 chain cluster,c – 13:4 Koch-Cohen cluster. Modified after.

a significant correlation between clusters was suggested [14]. At high pressures and in equilibrium with metallic Fe the degree of FeO non-stoichiometry decreases [15], implying that the stability of defect clusters changes significantly with pressure. Direct evidence for pressure-induced changes in the FeO defect structure were obtained from single crystal X-ray diffraction diffuse scattering observations [16].

The defect structure of FeO significantly influences its physical properties. It is known from many systematic studies that the lattice parameter varies linearly as a function of x in the $Fe_{1-x}O$ formula [17-18]. It is believed that the isothermal bulk modulus also depends on x, and this dependence is non monotonous [15,19]. Data on K and $K\prime$ from different studies are strongly scattered, however. Virtually nothing is known about the effect of ρ and defect cluster geometry and distribution on the elastic properties of FeO. Some atomistic semi-empirical simulations show that such correlations do exist [20]. These calculations imply that FeO samples with different synthesis temperatures and history (cooling rate, etc.) could show different elastic properties due to variations in ρ and cluster ordering even for similar x values. This could explain disagreements between different studies of FeO compressibility.

At low temperature near 90 K the FeO X-ray diffraction pattern is no longer consistent with ideal cubic symmetry, and a small degree of trigonal distortion has been observed [21]. Later a magnetic ordering (Néel) transition was also observed in FeO around 195 K, and structural distortion was assumed to be a magnetostriction effect, similar to MnO, CoO and NiO [22,23]. The magnetic structure of FeO at low temperature was one of the first structures solved by neutron diffraction [24]. Fe ions with parallel spins form flat sheets perpendicular to the <111> direction and the alternating sheets are antiparallel. A more recent high-resolution neutron diffraction study revealed that the crystal symmetry of nearly stoichiometric FeO is even lower (namely, monoclinic), which was attributed to the deviation of the spin orientation from the $< 111 >$ direction [25].

At high pressures a trigonal distortion and electronic transformations occur at room temperature. A trigonal distortion was observed at pressures from 9 to 24 GPa [26,27].The strongest effect on the transition pressure is when non-isotropic stress conditions are present in the sample : more hydrostatic conditions result in higher transition pressures [28].

At pressures above 90 GPa a structural phase transformation from the trigonal NaCl related structure to a NiAs-like hexagonal phase was observed [29]. Later it was discussed whether the observed diffraction pattern is consistent with a NiAs-like or an inverse NiAs-like structure, or even polytypical stacking of NiAs- and inverse NiAs-like layers [30].

Relations between the structural and electronic states of FeO in the high-pressure and high-temperature region still remain unclear.

1.2 Periclase and wüstite minerals

Periclase is the mineral name of MgO. Periclase is relatively scarce and is found mainly in marbles, and is usually formed during contact metamorphism of dolomites and magnesites. $CaMg(CO_3)_2$ dolomite dissociates into MgO (periclase), $CaCO_3$ (calcite) and CO_2 fluid. Pure MgO is colorless and transparent; however, natural crystals are usually yellow, brown or black due to the presence of iron. Specimens of periclase can be very attractive as brightly lustered, smoothly faceted crystals projecting out of the otherwise formless rough marble host rock. Periclase is an important industrial material, because it is formed in cements and is the basis of many high-temperature ceramics for a wide range of applications.

Wüstite (FeO) is a rare mineral of iron oxide found in meteorites with native iron and is isostructural to MgO at ambient conditions. Wüstite is a rather rare mineral, occurring in highly reducing environments. Under oxidizing conditions wüstite can be easily oxidized to various Fe^{3+} and mixed Fe^{2+} and Fe^{3+} oxides or hydroxides: magnetite Fe_3O_4, hematite Fe_2O_3, goethite FeO(OH), and so on. As mentioned above, wüstite never has the ideal FeO stoichiometry. In most natural and synthetic samples there is always a certain iron deficit that results in the chemical formula $Fe_{1-x}O$. Due to the presence of Fe^{3+} in the wüstite structure, strong charge transfer bands appear in the band structure, and bulk wüstite samples are opaque and black in color, while thin sections of wüstite are transparent [31].

At ambient conditions both MgO and FeO have a similar crystal structures, formal valence states and very close lattice parameters (about 4.212 Å for MgO and about 4.25 $\mathring{A}$ for FeO, depending on its stoichiometry). As a result, a complete series of $Mg_{1-x}Fe_xO$ solid solutions can be formed. The corresponding mineral form of $Mg_{1-x}Fe_xO$ is called ferropericlase for $x < 0.5$ and magnesiowüstite for $x > 0.5$ compositions. Although $Mg_{1-x}Fe_xO$ natural samples are rear on the Earth's surface, $Mg_{1-x}Fe_xO$ is believed to be one of the main constituents of the lower mantle and probably the most abundant oxide (non-silicate) phase on our planet according to current mineralogical models of the Earth.

A mineralogical model of the Earth predicts which minerals, their chemical compositions and abundances are present in different regions of the Earth's interior. A mineralogical model is the result of combining cosmochemical constrains with models of the Solar system and Earth formation, our understanding of the Earth's history, experimental and theoretical studies of thermodynamic phase stabilities over a wide pressure and temperature range, and geophysical (mostly seismological) data of elastic and other properties of the Earth's deep interior.

1.3 Chemical composition of the Earth's mantle: planet formation and the meteorite record

According to the current concepts, the formation of our solar system followed the collapse and fragmentation of a dense interstellar molecular cloud [32]. Due to angular momentum of this matter, a rotating disk was initially formed. Material within the disc lost its initial angular momentum through viscous dissipation of other processes, leading ultimately to the growth of a central star, our Sun. Only a tiny fraction of the mass of the solar system, about 0.1%, was left behind in the disc to form planets and asteroids. The mixture of gas and grains that made up the proto-solar accretion disk is called the solar Nebula.

The growth of solid bodies in the solar nebula began with the accretion of tiny dust grains. Initially micrometer-size grains gradually formed centimeter-size bodies that in turn

grew to meter- and kilometer-size blocks by collisional coagulation [33]. Once the diameter of the planetesimals had reached 1-10 km, gravitational forces controlled further growth. Three major conclusions derived from this model are most important for constraining bulk chemical composition of the Earth:

- Planetesimals appear to grow from small particles through a range of increasingly larger bodies. Planetesimals and planets do not grow by accreting dust onto a single nucleus.

- Bodies up to kilometer size are composed of the material derived from local matter sources and thus possess the chemical signatures characteristic to the heliocentric distance at which they formed.

- At some point there was a “cleaning” of the nebula through intense activity of the Sun, which removed gas and fine dust. This is the most probable mechanism for the removal of volatile elements. Earth group planets (Mercury, Venus, Earth and Mars) that are closer to the Sun lost a major part of their volatile elements, while more distant and heavy gas giants contains a much larger amount of volatile elements.

At the next step the inner planets were formed by accumulation of embryos. At this stage some mixing of embryos from different heliocentric distances occurred, and the material formed far out in the asteroid belt may have contributed significantly to the growing Earth and its chemistry.

During the formation of the solar system a certain heating and fractionation of chemical elements occurred. The cosmochemical behavior of an element depends mostly on two properties: its volatility in a gas of solar composition, and its affinity for metallic versus silicate or oxide phases. The cosmochemical classification of elements must include gas/solid or gas/liquid equilibria during initial condensation of the solar nebular (the element volatility) and metal/silicate or sulphide/silicate equilibria during metallic core formation. The latter type of partitioning divides elements into lithophile, siderophile and chalcophil. The distinction between the last two groups is of minor importance, since above the Fe-FeS eutectic temperature sulphide and metal melt to form a single S-containing metallic liquid.

Refractory elements have condensation temperatures higher than the major phases in meteorites (Mg silicates and FeNi metal) and make up about 5% of the condensable matter of the solar nebula. Condensation temperatures of refractories vary from 1800 to 1400 K.

The common or major elements Mg, Si, Cr, Fe, Ni, and Co have condensation temperatures only slightly lower than those of refractory elements (1300 – 1350 K), but condense in different phases. Mg and Si form forsterite Mg_2SiO_4 and enstatite $MgSiO_3$; whereas Fe, Ni, and Co condense as alloys. Silicate and metal phases together are the most important components forming planetesimals, accounting for at least 90% of chondritic meteorites. It is important that forsterite and metallic alloy have similar condensation temperatures, which explains the limited fractionation of metal and silicate phases in the solar nebula. Cr, according to recent thermodynamic data, mostly condenses to olivine and pyroxene as Cr_2SiO_4 and $CrSiO_3$ components. Mg and Si can be considered to be slightly volatile, relative to the refractory elements.

Volatile elements are those having condensation temperatures lower than those of Mg silicates and FeNi alloy. Volatiles can be lithophile, siderophile and chalcophile elements. They are depleted, relative to CI chondrites, in every other meteorite. There are no known examples of solar-system material with concentrations of volatile elements higher than the CI concentrations. This indicates that the depletion was not a simple local redistribution and also that it was fundamentally different to the siderophile element fractionation discussed in the preceding section, because the latter resulted in both metal-rich and metal-poor materials. Low volatile-element abundances are characteristic of the inner solar system, and the Earth should be no exception [34].

Ice-forming elements condense at temperatures below 300 K; these are H, C, N, and the rare gases. Only tiny fractions of the solar abundance of these elements are contained in even the most volatile-rich meteorites. The mechanism of ice-forming element depletion in the Earth is probably the same as for volatiles, but the degree of depletion is much higher. Oxygen has a unique status in cosmochemical classification due to its unique behavior. Some O was among the first material to condense with the refractory elements, and more condensed with Mg and Si. Next, more O condensed through oxidation of Fe metal, forming the FeO component of silicates and oxides. However, the amount of O condensing in this way is only ~15% of the solar nebula oxygen content. The remaining 85% of O is predicted to have condensed as H_2O in the ice-forming regime.

Although the meteoritic record provides a relatively well constrained bulk chemical composition of the Earth, the most important differentiation event inside the planet must be considered to understand its constitution. The fundamental division in the Earth is between its outer silicate portion, consisting of the mantle plus the crust which is usually called the Bulk Silicate Earth (BSE) and its Fe-rich metal core, which is 32% of the Earth by weight. An important issue regarding the principal divisions of the Earth is that the core is probably chemically isolated from the BSE and has been for most of the Earth's history. The justification for this view is the absence of any

Table 1.1: Table Major-element composition of the bulk silicate Earth (BSE), t – total iron content, is written as 'FeO',

Elem	O'Neill	Ringwood	Ringwood	Jagoutz	Wänke	Palme	Hart and
	and Palme			and al.	and al.	Nickel	Zindler
	(1998)	(1975)	(1979)	(1979)	(1984)	(1985)	(1986)
MgO	36.33	38.1	38.1	38.3	36.8	35.5	37.8
Al_2O_3	4.73	4.6	3.3	4.0	4.1	4.8	4.1
SiO_2	45.56	45.1	45.1	45.1	45.6	46.2	46.0
CaO	3.75	3.1	3.1	3.5	3.5	4.4	3.2
FeOt	8.17	7.9	8.0	7.8	7.5	7.7	7.5
Total	98.54	98.8	97.6	98.7	97.5	98.6	98.6

noticeable change in the siderophile element content of mantle-derived rocks with time over the entire geological record (i.e., from nearly 4.0 billion years ago).

The isolation of the core from the mantle means that the chemistry of the core is not accessible for direct investigation, except by imposing broad-scale constraints from geophysical observations such as density and seismic velocities. Rather, the chemistry of the core must be inferred from a global mass balance between the composition of the entire Earth, deduced from cosmochemical principles, and the composition of the BSE.

There are a number of independent estimations of BSE abundance of the elements (Table 1.1). For most elements, agreement among these estimates is good. The nature of the BSE composition determination is the following. The BSE is composed of a number of geochemical reservoirs: the continental crust; the sub-continental lithospheric mantle; the oceanic crust; the sub-oceanic lithosphere; the depleted, well-stirred upper mantle, which is the source region for mid-ocean-ridge basalt (MORB); the enriched, heterogeneous, source regions for ocean-island basalt (OIB), which may include subducted oceanic crust; and, possibly, primitive mantle that has never been differentiated. For a few extremely incompatible elements such as hydrogen, the noble gases, and Cl, Br, and I, the oceans and atmosphere also need to be included. The choice of what to define as a geochemical reservoir is somewhat arbitrary. For each element there is a mass balance that should be solved. Currently the BSE composition is known relatively well, and agreement between different workers is quite good (see Table 1.1).

It is remarkable that only five components constitute more than 98% of the bulk silicate Earth. This implies that a relatively simple model with a limited number of phases could be a relative good approximation for the bulk mantle composition. This idea is realized, in particular, in the well known pyrolite model of the mantle. The term 'pyrolite' was chosen by [35] as the name for a chemical composition of the mantle consisting predominantly of pyroxene and olivine. The pyrolite model is the most used and has been subsequently developed over the last few decades [36].

1.4 Geophysical record: seismic structure of the mantle

Seismological techniques have provided much of the currently available information on the internal structure of the Earth, and in particular on the mantle. Seismic waves, originating mainly from earthquakes, pass through the Earth while bouncing and refracting at seismic boundaries (Fig. 1.3). Analyzing and comparing seismograms from the same event recorded at different seismological stations allows the determination of

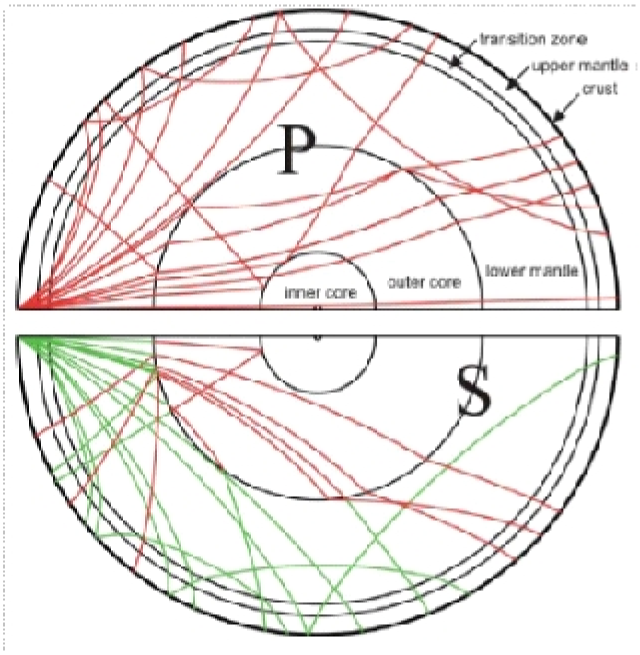

Figure 1.3: Scheme of different P- (upper hemisphere) and S- (lower hemisphere) seismic waves propagation paths through the Earth.

many physically important properties of the Earth: location of seismic boundaries and determination of seismic wave velocities, and pressures and densities in the deep interior. Early studies revealed the need for an increase in seismic velocity with depth in the Earth, and by 1915 Gutenberg was able to make a good estimate of the radius of the core based on seismic wave propagation though the Earth. Knowledge of the Earth's internal structure was refined by iterative improvement of earthquake locations and the travel times for seismic phases through the Earth, so that in 1940 Jeffreys and Bullen were able to publish an extensive set of travel time tables based on a model of both P-wave and S-wave velocities in the mantle.The presence of three-dimensional variations in the Earth's structure became apparent though regional differences in seismic travel times, and they became better understood once surface-wave observations demonstrated significant differences in surface-wave dispersion between oceanic and continental regions. Surface-wave studies revealed the presence of a zone of decreased shear-wave velocity at depth and showed significant variations in the thickness of the overlying high-velocity zone between different regions.

In last decades the quality and quantity of seismological data have improved sufficiently that it is possible to begin to resolve the three-dimensional structure within the Earth using a combination of information from the travel times for seismic phases, the free oscillations of the Earth, and long-period seismic waveforms. A consensus is developing regarding the largest-scale features in the aspherical structure. In particular, the upper mantle is a zone of major variability and relatively strong horizontal gradients in seismic properties. Subducted slabs are associated with large, localized contrasts in velocity. Detailed P-wave tomography based on the inversion of seismic travel times has revealed the complex patterns of subduction in many regions. The influence of subduction is largest in the upper mantle, but in many places subducted material appears to have penetrated directly or indirectly into the lower mantle.

The variation of seismic properties within the Earth is inferred from the analysis of seismograms in a variety of ways and is dominated by a radial dependence. However, three dimensional variations are manifest in the crust and in all parts of the mantle; currently the most effective representation of such three-dimensional structure is as a perturbation to a reference radial model. For this radial reference model, the major sources of information come from the travel times for seismic phases and from the free oscillations of the Earth. The travel times provide constraints on the seismic wave speeds within the Earth, and the frequencies of normal modes provide additional information on the density distribution and attenuation profile for seismic waves.

At present, nearly all the techniques designed to assess the three-dimensional structure of the Earth are based on a representation in terms of deviations from a reference model (which normally is a spherically symmetrical model). The nature of the reference model is therefore of considerable importance. These reference spherical models are also called one dimensional (1D) models [37] introduced a new style of representation for such reference models with the PEM model, which was defined in terms of a limited number of radial segments, within each of which the seismic velocities and densities were defined by polynomials (up to cubic) in radius.

1.5 Mineralogical model of the mantle. Ferropericlase in the Earth's deep interior

As shown above, there are strong pressure and temperature variations in the Earth's interior. Phase transformations in the main minerals are therefore quite possible and indeed are expected. Such transformations would have effects on density and/or on elastic properties. The potential consequences of density changes in terms of the dynamics of the Earth's mantle have been matters of active debate for at least 30 years [38]. There are formidable complexities in laboratory investigations of the mechanisms and kinetics describing transformations of mantle phases, as well as in the consequent geophysical interpretations. Nevertheless, many impressive successful studies have been made and are summarized briefly below. As mentioned above, the composition of bulk silicate Earth can be described fairly well as a mixture of olivine $(Mg,Fe)_2SiO_4$ and pyroxene $(Mg,Fe)SiO_3$, and phase transitions in these phases should be of the utmost importance.

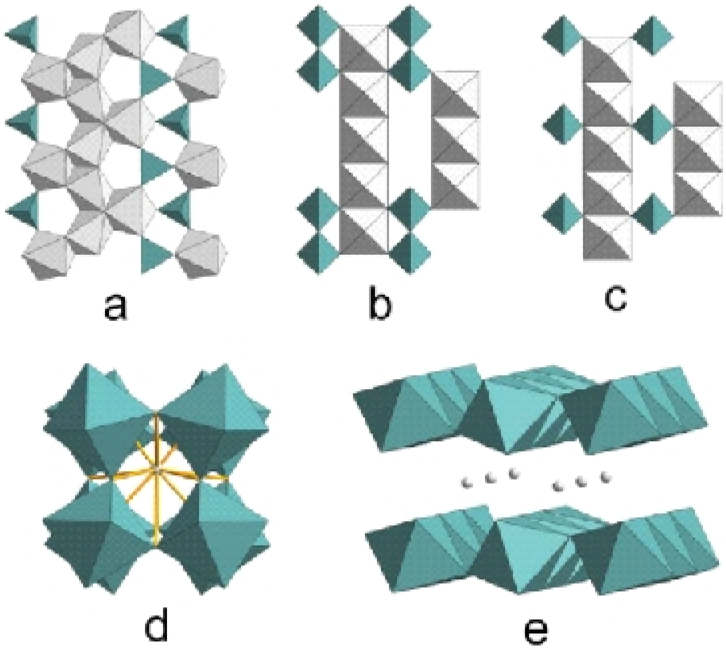

Figure 1.4: Polyhedral model of the crystal structures of Mg_2SiO_4 olivine (a), wadsleyite (b), ringwoodite (c) and $MgSiO_3$ perovskite (d) and "post-perovskite" (e).

$(Mg,Fe)_2SiO_4$.

Ringwood and Major [39] experimentally transformed the α phase (olivine) of $(Mg,Fe)_2SiO_4$ into its cubic spinel polymorph, now known as either the γ-phase or ringwoodite. In doing so, they noted the existence of a spinel-related phase, later named the β phase and given the mineral name wadsleyite. From crystal-structure determinations for these phases [40], it was shown that the β and γ phases are quite closely related, and both are significantly different from the α phase. Silicon is 4-coordinated and $[SiO_4]$ tetrahedra are isolated from each other (Fig. 1.4.a).

ringwoodite (c) and $MgSiO_3$ perovskite (d) and "post-perovskite" (e).Ringwoodite has a cubic spinel crystal structure with $[SiO_4]$ tetrahedra and $[MgO_6]$ octahedra (Fig.

1.4.c). This structure is denser compared to the α phase due to more effective space packing of [MgO_6] octahedra. The wadsleyite crystal structure is almost identical to the γ phase, but silicon tetrahedra forms isolated pairs that share a common apex (Fig. 1.4.b). Wadsleyite is also often called a “modified spinel” phase, compared to the “spinel” γ phase. All three phases have been shown to be thermodynamically stable in the Mg-Fe system with stability fields that are now experimentally well established.

The close relations between the β and γ phases have led many to conclude that the transition between these two phases can be accomplished by a diffusionless martensitic transformation [41]. In contrast, the transition from α to either α or γ must involve a major reconstruction of the polyhedral groupings and cation arrangements.

The nature of the phase-transition mechanisms likely to occur in $(Mg,Fe)_2SiO_4$ within the mantle above 660 km depth are fairly well understood. Our knowledge is now approaching the point where the kinetics of these transitions can be reasonably predicted and applied to the dynamics of subducted slabs.

The most important phase transition that is responsible for the 660-km discontinuity is the decomposition of ringwoodite into $(Mg,Fe)SiO_3$ with the perovskite structure and (Mg,Fe)O oxide. It is an important observation that equilibrium coexistence of these two phases is possible only above the transition pressure. Natural samples with coexisting (Mg,Fe)O and $(Mg,Fe)SiO_3$ (as pyroxene) in diamond inclusions are therefore concluded to have a lower mantle origin [42].

In the perovskite ABX3 structure cite the A site is 12-coordinated and the B site is six-coordinated (octahedral) by X anions (Fig. 1.4.d). [BX6] octahedra form a three-dimensional framework and share common apices. The A-cation occupies a large cavity in this framework. Perovskites can possess cubic symmetry or can be tetragonal, trigonal, orthorhombic or even monoclinic. In the latter cases, the A position is usually strongly distorted and its coordination number is more correctly written as 8 + 4, which means 8 X anions at somewhat shorter distances from the central A cation and 4 X anions at longer distances.

The term "perovskite" as applied to lower-mantle magnesium silicate is in some ways an unfortunate terminological choice. Perovskite is a relatively rare mineral with the chemical formula $CaTiO_3$. However there is an extremely broad range of chemical compounds that adopt the same or closely related crystal structures. There are several hundred synthetic compounds with the perovskite structure, and many of them have important technological applications. Hence the term perovskite is often used to denote a certain type of crystal structure. When it is applied to $MgSiO_3$, it could be somewhat confusing.

$(Mg,Fe)(Si,Al)O_3$

The second most abundant mineral in the pyrolite mantle model is pyroxene with the nominal formula $(Mg,Fe)SiO_3$. The pyroxene family features many textbook transformations that have long fascinated mineralogists. Angel and Hugh-Jones [43] reviewed the volume changes and phase relations among the ortho, high-clino, and low-clino polymorphs of enstatite. Hogrefe et al. [44] investigated the kinetics of transformation of $MgSiO_3$ at pressures of 16-21 GPa and reported that at 1000°C the high-clino polymorph of enstatite can undergo a non-equilibrium transition directly to a $MgSiO_3$ polymorph with the ilmenite ($FeTiO_3$) structure.

At moderate pressures in the presence of Al and Ca (which is the case for the mantle) pyroxene transforms to garnet. At the bottom of the upper mantle pyroxene is no longer stable, but only a mixture of garnet and $CaSiO_3$ perovskite. There is a possible cubic-tetragonal transition in $MgSiO_3$ majorite garnet as identified by microstructural effects [45], and the large volume change of about 16.9% for the $MgSiO_3$ end member [46] associated with the garnet- to-perovskite transition at the base of the mantle transition zone may be important. Because of the crystallographic complexities of some of the lower-pressure members of the $(Mg,Fe)(Si,Al)O_3$ family and the relatively high pressures of many of the transformations relevant to the deeper mantle, it is likely that detailed knowledge about transformations and their geophysical effects will remain limited, compared with those for the $(Mg,Fe)_2SiO_4$ minerals [47].

The discovery of another reconstructive phase transition that occurs in $MgSiO_3$ perovskite at pressures close to the core-mantle boundary provides more promising possibilities [48, 49]. This new phase has the $CaIrO_3$ layered structure which is not typical for high-pressure polymorphs in general. $[SiO_6]$ octahedra share a common edge, which creates columns and these columns are formed into layers by connecting through common apices. Mg and Fe ions are located in between adjacent Si-O layers (Fig. 1.4.e). Many speculations have been made regarding the possible implications of this transition on D" layer anomalies at the core-mantle boundary. For (Mg,Fe)O ferropericlase there are no structural phase transitions expected under mantle conditions. Although the FeO end-member of the solid solution undergoes certain phase transformations, the dilute (Mg,Fe)O solution has been assumed to exist in the cubic NaCl structure over the entire lower mantle P,T range [50]. The reconstructive phase transition from the NaCl-like structure to an NiAs-like structure in FeO at high pressures [29] could have a strong

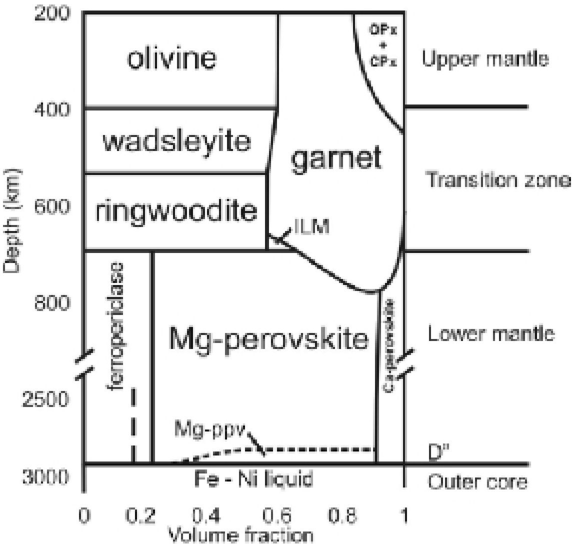

Figure 1.5: Volume fraction of the main rock-forming minerals of the Earth's mantle.

influence on the miscibility of MgO and FeO. In particular, at high pressures it could decompose into a Mg-rich cubic phase and a Fe-rich NiAs-like phase. Some experimental evidence for the decomposition of magnesiowüstite at high pressures and temperatures exist [51]. Surprisingly, the decomposition into two isostructural NaCl-like phases was observed, and the reason for MgO-FeO immiscibility was not clear. Moreover, some controversy still exists [50]. A schematic diagram showing the relative abundance of the different phases in the Earth's mantle summarizes all the above mentioned observations (Fig. 1.5).Conclusion

After having given a comprehensive survey of periclase and wustite physical properties in this chapter, we turned our attention to the chemical composition of the Earth's mantle. In this context a section has been devoted to the planet formation and the meteorite record followed by the seismological or geophysical one. As a result we presented the mineralogical model of the mantle and discussed the presence of ferropericlase in the Earth's deep interior. This is to link the seismological activity to the ferropericlase physical properties wich are the aim of the present work. The undertaken physical properties will be calculated in the frame work of the density functional theory (DFT). A description of this method is given in the next chapter.

BIBLIOGRAPHY

[1] T.S. Duffy, R.J.Hemley, H.K.Mao, Phys.Rev.Lett 74, (1995)1371.

[2] J.E.Jaffe, J.A.Snyder, Z. Lin, A.C.Hess Phys. Rev.B 62, (2000).

[3] J.Callaway, N.H.March, Density Functional Methods: Theory and Applications, Solid State Physics 38 (1984) 135.

[4] S.K.Saxena, N.Chatterjee, Y.Fei, and G. Thermodynamic Data on Oxides and Silicates. An Assessed Data Set Based on Thermochemistry and High Pressure Phase Equilibrium. Berlin, Springer-Verlag (1993).

[5] G. Chen, R.C. Liebermann, D.J. Weidner Elasticity of Single-Crystal MgO to 8 Gigapascals and 1600 Kelvin. Science 280, 1913, (1998).

[6] C.S.Zha, H.K.Mao, R.J. Elasticity of MgO and a primary pressure scale to 55 GPa. Proceedings of National Academy of Sciences USA 97, 13494, (2000).

[7] S. Speziale, C.-S. Zha, T.S.Duffy, R.J.Hemley, H.-K.Mao, Quasi-hydrostatic compression of magnesium oxide to 52 GPa: Implications for the pressure-volume temperature equation of state. Journal of Geophysical Research 106, 515 (2001).

[8] H.K.Mao, J.Shu, Y.Fei, J.Z.Hu, and R.J.Hemley The wüstite enigma. Physics of the Earth and Planetary Interior 96, 1351996.

[9] G.J.Long and F.Grandjean, Mössbauer effect, magnetic and structural studies of wüstite, Fe1-xO. Advances in Solid-State Chemistry 2, 187–221.

[10] J.Molenda, A.Stoklstrokosa, W.Znamirowski Physica Status Solidi B, 142, (1987) 517.

[11] S.Mrowec, A.Podgorecka. Journal of Materials Science 22, (1987)4181.

[12] W.L.Roth. Acta Crystallographica 13, (1960)140.

[13] F.Koch and J.B.Cohen. Acta Crystallographica B 25,(1969)275.

[14] T.R.Welberry and A.G.Christy. Physics and Chemistry of Minerals 24, (1997)24.

[15] C.McCammon. Science 259, (1993)66.

[16] Y.Ding, H.Liu, M. Somayazulu, Y.Meng, J.Xu, C.T.Prewitt, R.J.Hemley, H.K.Mao. Phy.Rev B 72, (2005) 174109.

[17] B.Simons. Composition – Lattice Parameter Relationship of the Magnesiowüstite Solid Solution Series. Carnegie Institution of Washington Yearbook 79, 376-380, (1980).

[18] C.A.McCammon and L.-G.Liu. The effects of pressure and temperature on nonstoichiometric wüstite, FexO: The iron-rich phase boundary. Physics and Chemistry of Minerals 10, 106-113, (1984).

[19] J.Zhang. Phys. Rev.Lett. 84, (2000) 507.

[20] C.Haavik, S. Stolen, M. Hanfland, C.R.A. Catlow. Physical Chemistry - Chemical Physics 2, (2000)5333.

[21] B.T.M.Willis and H.P.Rooksby. Acta Crystallographica 6, (1953) 827.

[22] J.S.Smart and S.Greenwald. Phys.Revi 82, (1951) 113.

[23] C.A. McCammon. Journal of Magnetism and Magnetic Materials 104-107, (1992) 1937

[24] C.G Shull, W.A.Strauser, and O.E.Wollan. Phys.Rev 83, (1951) 333-345.

[25] H.Fjellvag, B.C.Hauback, T.Vogt, and S.Stolen. Monoclinic nearly stoichiometric wüstite at low temperatures. American Mineralogist 87, (2002) 347.

[26] G.Zou, H.K.Mao, P.M.Bell and D.Virgo. High-pressure experiments on the iron oxide wüstite (Fe1-xO). Carnegie Institution of Washington Yearbook 79, 374-376, (1980).

[27] S.D.Jacobsen, J.F.Lin, R.J.Angel, G.Shen, V.B. Prakapenka, P.Dera, H.K.Mao, and R.J.Hemley. Single-crystal synchrotron X-ray diffraction study of wüstite and magnesiowüstite at lower-mantle pressures. Journal of Synchrotron Radiation 12, 577-583. (2005)

[28] L.Dubrovinsky, N.Dubrovinskaia, S.Saxena, T.LiBehan. Material Sciences and Engineering A 288, (2000-II) 187.

[29] Y.Fei and H.K.Mao. Science 266, (1994)1678.

[30] I.I.Mazin, Y.Fei, R.Downs, and R.E.Cohen. American Mineralogist 83, (1998) 451

[31] J. W.Anthony, R.A.Bideaux, K.W.Bladh, M.C.Nichols. Handbook of Mineralogy, volume III - Halides, Hydroxides, Oxides. Mineral Data Publishing, Tucson, 628 p

[32] H.St.C.O'Neill and H.Palme. Composition of the Silicate Earth: Implications for Accretion and Core Formation. In: The Earth's Mantle, ed. I. Jackson, pp. 3-127. Cambridge University Press. (1998)

[33] S.J.Weidenschilling. Formation processes and time scales for meteorite parent bodies.In: Meteorites and the Early Solar System, ed. J.F. Kerridge and M.S. Matthews, pp. 348-371. Tucson: University of Arizona Press (1998) .

[34] H.Palme, J.Larimer, and M.E.Lipschutz. Moderately volatile elements. In: Meteorites and the Early Solar System, ed. J.F. Kerridge and M.S. Matthews, pp. 436-461.University of Arizona Press, Tucson. (1988)

[35] A.E.Ringwood. Journal of Geophysical Research 67, (1962)857.

[36] D.H.Green, T.J.Falloon Pyroline: A Ringwood Concept and Its Current Expression.In: The Earth's Mantle, ed. I. Jackson, pp. 311-378. Cambridge University Press.

[37] A.M.Dziewonski, A.L.Hales, and E.R.Lapwood. Physics of the Earth and Planetary Interior 10, (1975) 12.

[38] A.E.Ringwood. New York: McGraw-Hill(1975).

[39] A.E. Ringwood and A.Major. Earth and Planetary Science Letters 1, (1996)241.

[40] N.Morimoto, S.Akimoto, K.Koto, and M.Tokonami. Physics of the Earth and Planetary Interior 3, (1970) 161-165.

[41] G.D.Price. Physics of the Earth and Planetary Interior 33,137-147,(1983).

[42] B.Harte, and Harris. Mineralogical Magazine A 58, (1994) 384.

[43] R.J.Angel and Hugh-Jones. Journal of Geophysical Research. 99, (1994) 19777.

[44] A.Hogrefe, D.C.Rubie, T.G.Sharp, and F.Seifert. Nature. 372, (1994) 351.

[45] T.G.Sharp and D.C.Rubie. Science 269, (1995)1095.

[46] H.Yusa, M. Akaogi, and E.Ito. . Journal of Geophysical Research. 98, (1993) 409.

[47] M.R.Drury and J.D.Fitz. Geophysical Research Letters 23, (1996) 701-704

[48] M.Murakami, K. Hirose, K. Kawamura, N.Sata, Y.Ohishi. Post-Perovskite Phase Transition in MgSiO3. Science 304, 855-858, (2004)

[49] A.R.Oganov and S.Ono. Theoretical and experimental evidence for a post-perovskite phase of MgSiO3 in Earth's D" layer. Nature 430, 445-448, (2004)

[50] J.-F.Lin, D.L.Heinz, H.K.Mao, R.J.Hemley, Devine, J.Li, and G.Shen Proc.Nati.Acad.Scie USA 100, Stability of magnesiowustite in Earth's lower mantle. Proceedings of National Academy of Sciences USA 100, 4405-4408 2003)

[51] L.S.Dubrovinsky, N.A.Dubrovinskaia, S.K.Saxena, H.Annersten, E.Hålenius, H.Harryson, F.Tutti, S.Rekhi, T.Le Bihan. Stability of Ferropericlase in the Lower Mantle.Science 289, 430-432. (2000-I).

CHAPTER 2

DENSITY FUNCTIONAL THEORY

2.1 Introduction

For the past 30 years, density functional theory has been the dominant method for the quantum mechanical simulation of periodic systems. In recent years it has also been adopted by quantum scientists and is now very widely used for the simulation of materials properties. In this chapter we introduce the basic concepts underlying density functional theory and outline the features that have lead to its wide spread adoption. Recent developments in exchange correlation functionals are introduced and the performance of families of functionals is addressed.

2.2 The Solution of Schrödinger Equation

In this section we will be primarily concerned with calculation of the ground state energy of a collection of atoms. The energy may be computed by solution of the Schrödinger equation:

$$\widehat{H}\Psi\left(r_1, r_2, ...r_N\right) = E\Psi\left(r_1, r_2, ..., r_N\right) \tag{2.1}$$

$$\widehat{\hat{H}} = \frac{1}{2}\sum_{i}^{N}\nabla_i^2 + \widehat{V}_{ext} + \sum_{I \prec J}^{N}\frac{1}{\left|r_1 - r_2\right|} \tag{2.2}$$

In materials simulation the external potential of interest is simply the interaction of the electrons with the atomic nuclei;

$$\widehat{V}_{ext} = \sum_{\alpha}^{N_{at}} \frac{1}{|r_i - R_\alpha|}. \tag{2.3}$$

Here, r, is the coordinate of electron i and the charge on the nucleus at R_α is Z_α. Note that in order to simply the notation and to focus the discussion on the main features of DFT the spin coordinate is omitted here and throughout this chapter.

Equation 2.1 is solved for a set of Ψ subject to the constraint that they the Ψ are anti-symmetric they change sign if the coordinates of any two electrons are interchanged. The lowest energy eigenvalue, E_0,is the ground state energy and the probability density of finding an electron with any particular set of coordinates $\{r_i\}$ is $|\Psi_0|^2$.

The average total energy for a state specified by a particular Ψ,not necessarily one of the eigenfunctions of equation 2.1, is the expectation value of H, that is;

$$E\left[\Psi\right] = \int \Psi^* \widehat{H} \Psi dr \equiv \left\langle \Psi \left| \widehat{H} \right| \Psi \right\rangle \tag{2.4}$$

The notation $[\Psi]$ emphasises the fact that the energy is a functional of the wave function. The energy is higher than that of the ground state unless Ψ corresponds to $\Psi_0$which is the variational theorem;

$$E\left[\Psi\right] \succeq E_0 \tag{2.5}$$

The ground state wave function and energy may be found by searching all possible wavefunction for the one that minimizes the total energy. Hartree-Fock theory consists of an ansatz for the structure of Ψ- it is assumed to be an an antisymmetric product of functions (ϕi) each of which depends in the coordinates of a single electron, that is;

$$\Psi_{HF} = \frac{1}{\sqrt{N!}} \det \left[\phi_1 \phi_2 \phi_3 .....\phi_N\right] \tag{2.6}$$

Where, det indicates a matrix determinant [1]. Substitution of this ansatz for Ψ into the schrodinger equation results in an expression for the Hartree Fock energy;

$$E_{HF} = \int \phi_i^* \left(r\right) - \left(\frac{1}{2} \sum_i^N \nabla_i^2 + V_{ext}\right) \phi_i \left(r\right) dr$$

$$+\frac{1}{2} \sum_{i,j}^N \int \frac{\phi_i^* \left(r_1\right) \phi_1 \left(r_1\right) \phi_j^* \left(r_2\right) \phi_j \left(r_2\right)}{\left|r_i - r_j\right|} dr_1 dr_2$$

$$-\frac{1}{2} \sum_{i,j}^N \int \frac{\phi_i^* \left(r_1\right) \phi_j \left(r_1\right) \phi_i \left(r_2\right) \phi_j^* \left(r_2\right)}{\left|r_i - r_j\right|} dr_1 dr_2 \tag{2.7}$$

The second term is simply the classical Coulomb energy written in terms of the orbitals and the third term is the exchange energy.

The ground state orbitals are determined by applying the variation theorem to this energy expression under the constraint that the orbitals are orthonormal. This leads to the Hartree-Fock (or SCF) equation;

$$\left[-\frac{1}{2}\nabla^2 + v_{ext}(r) + \int \frac{\rho\left(\acute{r}\right)}{\left|r - \acute{r}\right|} d\acute{r}\right] \phi_i \left(r\right) + \int v_X \left(r, \acute{r}\right) \Phi_i \left(\acute{r}\right) d\acute{r} = \varepsilon_i \Phi_i(r) \tag{2.8}$$

where the non-local exchange potential, v_X, is such that:

$$\int v_X \left(r, \acute{r}\right) \Phi_i \left(\acute{r}\right) d\acute{r} = -\sum_j^N \int \frac{\Phi_j \left(r\right) \Phi_j^* \left(\acute{r}\right)}{\left|r - \acute{r}\right|} \Phi_i \left(r\right) d\acute{r} \tag{2.9}$$

The Hartree-Fock equations describe non-interacting electrons under the influence of a mean field potential consisting of the classical Coulomb potential and a non-local exchange potential.

From this starting point better approximation (correlated methods) for Ψ and E_0 are readily obtained but the computational cost of such improvements is very high and scales prohibitively quickly with the number of electrons treated. In addition, accurate solutions require a very flexible description of the wavefunction's spatial variation, i.e. a large and basis set is required which also adds to the expense for practical calculations. Many correlated methods have been developed for molecular calculations [1].

The discussion above has established that direct solution of the Schrodinger equation is not currently feasible for systems of interest in condensed matter science. This is a major motivation for the development and used of density functional theory. The question that arises is : Is it necessary to solve the schrodinger equation and determine the 3N dimensional wavefunction in order to compute the ground state energy ?

2.3 Avoiding the solution of the Schrodinger Equation

The Hamiltonian operator 2.2 consists of single electron and bi-electronic interactions i.e. operators that involve on the coordinates of one or two electrons only. In order to compute the total energy we do not need to know the 3N dimensional wavefunction. Knowledge of the two-particle probability density – that is, the probability of finding an electron at r_1 and an electron at r_2 is sufficient.

A quantity of great use in analysing the energy expression is the second order density matrix, which is defined as:

$$P_2\left(\acute{r}_1,\acute{r}_1;r_1,r_{\acute{e}}\right)=\frac{N\left(N-1\right)}{2}\int\Psi^*\left(\acute{r}_1,\acute{r}_1,....,\acute{r}_N\right)$$

$$\Psi\left(r_{1,}r_{2,}....,r_N\right)dr_3dr_4....dr \tag{2.10}$$

The diagonal elements of p_2,often referred to as the two-particle density matrix or pair density, are;

$$P_2\left(r_{1,}r_2\right)=P_2\left(r_{1,}r_2;r_{1,}r_2\right) \tag{2.11}$$

This is the required two electron probability function and completely determined exactly;

$$E=tr(\widehat{H}\widehat{P})=\int\left[\left(-\frac{1}{2}\nabla_1^2-\sum_{\alpha}^{Nat}\frac{Z_\alpha}{|r_1-R_\alpha|}\right)P_1\left(\acute{r_1},r_2\right)\right]_{r_1-r_2}dr$$
$$+\int\frac{1}{|r_1-r_2|}P_2\left(r_1,r_2\right)dr_1dr_2 \tag{2.12}$$

2.4 The Hohenburg-Kohn Theorems

In 1964 Hohenburg and Kohn proved the two theorems [2]. The first theorem may be stated as follows : The electron density determines the external potential (to within an additive constant).If this statement is true then it immediately follows that the electron density uniquely determines the Hamiltonian operator. This follows as the Hamiltonian is specified by the external potential and the total number of electrons, N, which can be computed from the density simply by integration over all space. Thus, in principle, given the charge density, the Hamiltonian operator could be uniquely determined and this wave functions Ψ (of all states) and all material properties computed.

Hohenberg and Kohn [2] gave a straightforward proof of this theorem, which was generalized to include systems with degenerated states in proof given by Levy in 1979 [3]. It is said that the theoretical spectroscopist E.B. Wilson put forward a very straightforward proof of this theorem during a meeting in 1965 at which it was being introduced. Wilson's observation is that the electron density uniquely determines the positions and charges of the nuclei and thus trivially determines the Hamiltonian. This proof is both transparent and elegant – it is based on the fact that the electron density has a cusp at the nucleus, such that;

$$Z_\alpha = \frac{-1}{2\overline{\rho}\left(0\right)}\left[\frac{\partial\overline{\rho}\left(r_\alpha\right)}{\partial r_\alpha}\right]_{r_\alpha=0} \tag{2.13}$$

where $\overline{\rho}\left(r\right)$is the spherical average of ρ and so a sufficiently careful examination of the charge density uniquely determines the external potential and thus the Hamiltonian.

Although less general than the Levy proof this observation establishes the theorem for the case of interest – electrons interacting with nuclei. The first theorem may be summarized by saying that the energy is a functional of the density - $E\left[\rho\right]$.

The second theorem establishes a variational principle;

For any positive definite trial density, ρ_t such that

$$\int \rho_t\left(r\right) = N then E\left[\rho_t\right] \succeq E_0$$

The proof of this theorem is straightforward. From the first theorem we know that the trial density determines a unique trial Hamiltonian (H_t) and thus wavefunction (Ψ_t);$E\left[\rho_t\right] = \left\langle \Psi_t \left| H \right| \Psi_t \right\rangle \succeq E_0$ follows immediately from the variational theorem of the Schrodinger equation 2.2. This theorem restricts density functional theory to studies of the ground state. A slight extension allows variation to excited states that can be guaranteed orthogonal to the ground state but in order to achieve this knowledge of the exact ground state wavefunction is required.

The two theorems lead to the fundamental statement of density functional theory;

$$\delta \left[E\left[\rho\right] - \mu \left(\int \rho\left(r\right) dr - N \right) \right] = 0 \tag{2.14}$$

The ground state energy and density correspond to the minimum of some functional $E\left(\rho\right)$ Subject to the constraint that the density contains the correct number of electrons. The Lagrange multiplier of this constraint is the electronic chemical potential μ

The above discussion establishes the remarkable fact that there is a universal functional $E\left[\rho\right]$ (i.e. it does not depend on the external potential which represents the particular system of interest) which, if we knew its form, could be inserted into the above equation and minimized to obtain the exact ground state density and energy.

2.5 The Energy Functional

From the form of the Schrodinger equation 2.1 we can see that the energy functional contains three terms – kinetic energy, the interaction with the external potential and the electron-electron interaction and so we may write the functional as;

$$E\left[\rho\right] = T\left[\rho\right] + V_{ext}\left[\rho\right] + V_{ee}\left[\rho\right] \tag{2.15}$$

The interaction with the external potential is trivial;

$$V_{ext}\left[\rho\right] = \int V_{ext}\rho\left(r\right)dr \tag{2.16}$$

The kinetic and electron-electron functionals are unknown. If good approximations to these functional could be found direct minimization of the energy would be possible; this possibility is the subject of much current research – see for instance Ref. [4]

Kohn and Shan proposed the following approach to approximating the kinetic and electron-electron functional [5]. They introduced a fictitious system of N non-interacting electrons to be described by a single determinant wavefunction in N "orbitals" ϕ_i. In this system the kinetic energy and electron density are known exactly from the orbitals;

$$T_s\left[\rho\right] = -\frac{1}{2}\sum_i^N \left\langle \phi_i \left| \nabla^2 \right| \phi_i \right\rangle \tag{2.17}$$

Here the suffix emphasises that this is not the true kinetic energy but is that of a system of nono-interacting electrons, which reproduce the true ground state density,

$$\rho\left(r\right) = \sum_i^N \left|\phi_i\right|^2 \tag{2.18}$$

The construction of the density explicitly from a set of orbitals ensures that it is legal – it can be constructed from an asymmetric wavefunction. If we also note that a significant component of the electron-electron interaction will be the classical Coulomb interaction – or Hartree energy (this is simply the second term of equation 2.7 written in terms of the density);

$$V_H\left[\rho\right]=\frac{1}{2}\int\frac{\rho\left(r_1\right)\rho\left(r_2\right)}{\left|r_{1-}r_2\right|}dr_1dr_2 \tag{2.19}$$

The energy functional can be rearranged as;

$$E\left[\rho\right]=T_S\left[\rho\right]+V_{ext}\left[\rho\right]+V_H\left[\rho\right]+E_{XC}\left[\rho\right] \tag{2.20}$$

Where we have introduced the exchange-correlation functional;

$$E_{xc}\left[\rho\right]=\left(T\left[\rho\right]-T_S\left[\rho\right]\right)+\left(V_{ee}\left[\rho\right]-V_H\left[\rho\right]\right) \tag{2.21}$$

E_{xc} is simply the sum of the error made in using a non-interacting kinetic energy and the error made in treating the electron-electron interaction kinetic energy and the error made in treating the electron-electron interaction classically.

Writing the functional 2.15 explicitly in terms of the density built from non-interacting orbitals 2.14 and applying the variational theorem 2.13 we find that the orbitals, which minimize the energy, satisfy the following set of equation;

$$\left[-\frac{1}{2}\nabla^2+v_{ext}\left(r\right)+\int\frac{\rho\left(\acute{r}\right)}{\left|r-\acute{r}\right|}d\acute{r}+v_{xc}\left(r\right)\right]\Phi_i\left(r\right)=\varepsilon_i\Phi_i\left(r\right) \tag{2.22}$$

In which we have introduced a local multiplication potential which is the functional derivative of the exchange correlation energy with respect to the density,

$$v_{xc}\left(r\right)=\frac{\delta E_{xc}\left[\rho\right]}{\delta\rho} \tag{2.23}$$

This set of non-linear equations (the Kohn-Sham equations) describes the behaviour of non-interacting ”electron” in an effective local potential. For that exact functional, and thus exact local potential, the "orbitals" yield the exact ground state density via Equation 14 and exact ground state energy via Equation 2.15. These Kohn-Sham equations have the same structure as the Hartree-Fock equations (Equation 2.8) with the non-local exchange potential replaced by the local exchange-correlation potential v_{xc}. We note at this point that the nomenclature in general use and reproduced here is very misleading. As stated above E_{xc} contains an element of kinetic energy and is not the sum of the exchange and correlation energies as they are understood in Hartree-Fock and correlated wavefunction theories.

The Kohn-Sham approach achieves an exact correspondence of the density and ground state energy of a system consisting of non-interacting Fermions and the "real" many body system described by Schrodinger equation. A cartoon representing this relationship is displayed in Fig 2.1.

The correspondence of the charge density and energy of the many-body and the non-interacting system is only exact if the exact functional is known. In this sense Kohn-Sham density functional theory is an empirical methodology – we do not know (and have no way of systematically approaching) the exact functional. However, the functional is universal – it does not depend on the materials being studied. For any particular system we could, in principle solve the Schrodinger equation exactly and determine the energy functional and its associated potential. This, of course, involves a greater effort than a direct solution for the energy. Nevertheless, ability to determine exact properties of the universal functional in a number of system allows excellent approximations to the functional to be developed and used unbiased and thus predictive studies of a wide range of materials – a property usually associated with an ab initio theory. For this reason

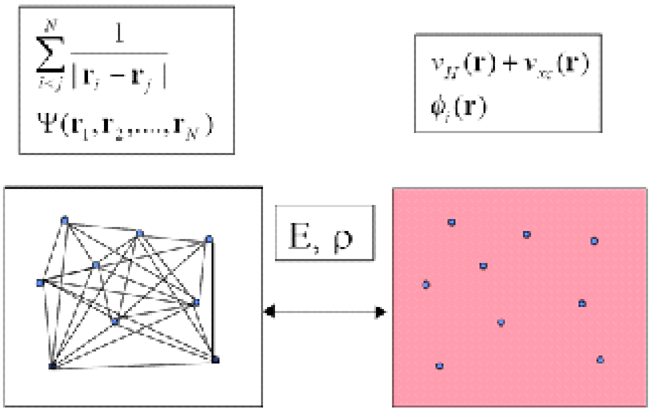

Figure 2.1: A cartoon representing the relationship between the "real" many body system (left hand side) and the non-interacting system of Kohn Sham density functional theory (left hand side) and the non-interacting system of Kohn Sham density functional theory (right hand side).

the approximations to density functional theory discussed below are often referred to as ab initio or first principles methods.

The computational cost of solving the Kohn Sham equations(Equation 2.16) scales formally as N3 (due to the need to maintain the orthogonality of N orbitals) but in current practice is dropping towards N1 through the exploitation of the locality of the orbitals.For calculation in which the energy surface is the quantity of primary interest DFT offers a practical and potential highly accurate alternative to the wavefunction methods discussed above. In practice, the utility of the theory rests on the approximation used for $E_{xc}[\rho]$

2.6 The Local Density Approximation for $E_{xc}[\rho]$

The generation of approximation for E_{xc} has lead to a large and still rapidly expanding field of research. There are now many different flavours of functional available which are more or less appropriate for any particular study. Ultimately such judgment must be made in terms of results (i.e.: the direct comparison with more accurate theory or experimental data, which will be discussed below) but knowledge of the derivation and structure of functional is very valuable when selecting which to use in any particular study. The early thinking that lead to practical implementations of density functional theory was dominated by one particular system for which near exact results could be obtained – the homogenous electron gas. In this system the electrons are subject to a constant external potential and thus charge density is constant. The system is thus specified by a single number – the value of the constant electron density $= \frac{N}{V}$.

Thomas and Fermi studied the homogeneous electron gas in the early 1920's [6]. The orbitals of the system are, by symmetry, plane waves. If the electron-electron interaction is approximated by the classical Hartree potential (that is exchange and correlation effects are neglected) then thetotal energy functional can be readily computed [6]. Under these conditions the dependence of the kinetic and exchange energy (Equation 2.7) on the density of the electron gas can be extracted (Dirac [7,8,9]) and expressed in terms of a local functions of the density. This suggests that in the inhomogeneous system we might approximate the functional as an integral over a local function of the charge density. Using the kinetic and exchange energy densities of the non-interacting homogenous electron gas this leads to;

$$T\left[\rho\right] = 2.87 \int \rho^{\frac{5}{3}}\left(r\right) dr \tag{2.24}$$

and,

$$E_x\left[\rho\right] = 0.74 \int \rho^{\frac{5}{3}}\left(r\right) dr \tag{2.25}$$

These results are highly suggestive of a representation for E_{xc} in an inhomogeneous system. The local exchange correlation energy per electron might be approximated as a simple function of the local charge density (say, $\varepsilon_{xc}\left(\rho\right)$). That is, an approximation of the form;

$$E_{XC}\left[\rho\right] \approx \int \rho\left(r\right) \varepsilon_{xc}\left(\rho\left(r\right)\right) dr \tag{2.26}$$

An obvious choice is then to take $\varepsilon_{xc}\left(\rho\right)$ to be the exchange and correlation energy density of the uniform electron gas of density ρ – this is the local density approximation (LDA). Within the LDA $\varepsilon_{xc}(\rho)$ is a function of only the local value of the density. It can be separated into exchange and correlation contributions;

$$\varepsilon_{xc}\left(\rho\right) = \varepsilon_x\left(\rho\right) + \varepsilon_c\left(\rho\right) \tag{2.27}$$

The Dirac form can be used for ε_x (Equation)

$$\varepsilon_x\left(\rho\right) = -C\rho^{\frac{1}{3}} \tag{2.28}$$

Where for generality a free constant, C, has been introduced rather than that determined for the homogeouns electron gas. This functional form is much more widely applicable than is implied from its derivation and can be established from scaling arguments [8]. The functional form for the correlation energy density, ε_x, is unknown and has been simulated for the homogeneous electron gas in numerical quantum Monte Carlo calculations which yied essentially exact results [10]. The resultant exchange correlation energy has been fitted by a number of analytic forms [11,12,13] all of which yield similar results in practice and are collectively referred to as LDA functional.

We can conclude that the remarkable performance of the LDA is a consequence of its reasonable description of the spherically averaged exchange correlation hole coupled with the tendency for errors in the exchange energy density to be cancelled by errors in the correlation energy density. An understanding of the these features is an important pre-requisite to developing functional that seek to improve on the LDA.

2.7 The Generalized Gradient Approximation

The local density approximation can be considered to be the zeroth order approximation to the semi-classical expansion of the density matrix in terms of the density and its derivatives [14]. A natural progression beyond the LDA is thus to the gradient expansion approximation (GEA) in which first order gradient terms in the expansion are included. This results in an approximation for the exchange hole [14] which has a number of unphysical properties; it does not normalize to -1, it is not negative definite and it contains oscillations at large u [15]. In the generalized gradient approximation (GGA) a functional form is adopted which ensures the normalization condition and that the exchange hole is negative definite [16,17]. This leads to an energy functional that depends on both the density and its gradient but retains the analytic properties of the exchange correlation hole inherent in the LDA. The typical form for a GGA functional is;

$$E_{xc} \approx \int \rho\left(r\right) \varepsilon_{xc}\left(\rho, \nabla\rho\right) dr \tag{2.29}$$

As we will see below the GGA improves significantly on the LDA's description of the binding energy of molecules – it was this feature which lead to the very wide spread acceptance of DFT in the chemistry community during the early 1990's. A number of functional within the GGA family [16,17,18,19,20,21] have been developed. The performance of these functional will be discussed below.

2.8 Meta-GGA functional

Recently functional that depend explicitly on the semi-local information in the Laplacian of the spin density or of the local kinetic energy density have been developed [22,23,24]. Such functional are generally referred to as meta-GGA functional. The form of the functional is typically;

$$E_{xc} \approx \int \rho\left(r\right) \varepsilon_{xc}\left(\rho, \left|\nabla_{\rho}\right|, \nabla^2\rho, \tau\right) dr \tag{2.30}$$

Where the kinetic energy density τ is;

$$\tau = \frac{1}{2}\sum\left|\nabla\varphi_i\right|^2 \tag{2.31}$$

2.9 Hybrid Exchange Functional

There is an exact connection between the non-interacting density functional system and the fully interacting many body system via the integration of the work done in gradually turning on the electron-electron interactions. This adiabatic connection approach [25] allows the exact functional to be formally written as:

$$E_{xc} = \frac{1}{2}\int \overrightarrow{dr}\,\overrightarrow{d\acute{r}} \int_{\lambda=0}^{1} d\lambda \frac{\lambda e^2}{\left|\overrightarrow{dr} - \overrightarrow{d\acute{r}}\right|}$$

$$\left[\left\langle \rho\left(\overrightarrow{r}\right)\rho\left(\overrightarrow{\acute{r}}\right)\right\rangle_{\rho,\lambda} - \rho\left(\overrightarrow{r}\right)\delta\left(\overrightarrow{r} - \overrightarrow{\acute{r}}\right)\right] \tag{2.32}$$

Where the expectation value $\langle ... \rangle_{\rho,\lambda}$ is the density-density correlation function and is computed at density $\rho\left(r\right)$ for a system described by the effective potential,

$$V_{eff} = V_{en} + \frac{1}{2}\sum_{i \neq j} \frac{\lambda e^2}{\left|\overrightarrow{r_l} - \overrightarrow{r_j}\right|} \tag{2.33}$$

Thus the exact energy could be computed if one knew the variation of the density-density correlation function with the coupling constant, λ. The LDA is recovered by replacing the pair correlation function with that for the homogenous electron gas. The adiabatic integration approach suggests a different approximation for the exchange-correlation functional. At $\lambda = 0$ the non-interacting system corresponds identically to the Hartree-Fock ansatz, while the LDA and GGA functional are constructed to be excellent approximations for the fully interacting homogeneous electron gas – that is, a system with $\lambda = 1$. It is therefore not unreasonable not unreasonable to approximate the integral over the coupling constant as a weighted sum of the end points – that is, we might set:

$$E_{xc} \approx aE_{Fock} + bE_{xc}^{GGA}$$

With the coefficient are to be determined by reference to a system for with the exact result is known. Becke adopted this approach [26] in the definition of a new functional with coefficients determined by a fit to the observed atomization energies, ionisation potentials, proton affinities and total atomic energies for a number of small molecules [26]. The resultant (three parameter) energy functional is,

$$E_{xc} = E_{xc}^{LDA} + 0.2\left(E_X^{Fock} - E_X^{LDA}\right) + 0.72\Delta E_X^{B88} + 0.81\Delta E_C^{PW91} \tag{2.34}$$

Here ΔE_X^{B88} and widely used GGA corrections [27,28] to the LDA exchange and correlation energies respectively.

Hybrid functional of this type are now very widely used in chemical applications with the B3LYP functional (in which the parameterization is as given above but with a different GGA treatment of correlation [29] being the most notable. Computed binding energies, geometries and frequencies are systemtically more reliable than the best GGA functional.

2.10 Successes and failures of DFT

DFT, even in the simplest LDA approximation, turns out to be much more successful than expected. Especially for solids, LDA is computationally much simpler than HF with the true exchange potential and no more complex than Slater's local exchange approximation. Yet, LDA yields results that compare well to HF results, even in atoms and molecules – highly inhomogeneous systems for which an approximation based on the homogeneous electron gas would hardly look appropriate. The best results are however obtained in solids, whose structural and vibrational properties are in general well described: the correct crystal structure is usually found to have the lowest energy; bond lengths, bulk moduli, phonon frequencies are accurate within a few percent.

One may wonder why LDA is so successful, given its resemblance with the not-sopraised Slater approximation to HF. One reason is somewhat fortuitous: LDA contains a fair amount of error compensation between the exchange and correlation parts. LDA grants a good description of the spherical term of the so-called "exchange-correlation hole". LDA also has some well-known serious problems. Some can be avoided by using better functionals, some others have a deeper and more fundamental nature.

2.11 Conclusion

Density functional theory provides us with a relatively efficient and unbiased tool with. Which to compute the ground state energy in realistic models of bulk materials and their surfaces. The reliability of such calculations depends on the development of approximations for the exchange-correlation energy functional. Significant advances have been made in recent years in the quality of exchange correlation functionals as dependence on local density gradients. We do have calculated the structural, optoelectronic and elastic properties of our $\mathrm{Mg}_{1-x}\mathrm{Fe}_x\mathrm{O}$ alloys in the frame work of this theory. The major obtained results of our study are to be presented in the following chapter.

BIBLIOGRAPHY

[1] A.Szabo, N.S.Ostlund, Modern Quantum Chemistry, McMillan, New York, 1982.

[2] P.Hohenburg and W.Kohn, Phys. Rev. B 136 (1964) 864.

[3] M.Levy and J.P.Perdew, The Constrained Search Formalism for Density Functional Theory, in Density Functional Methods in Physics, Ed. R.M.Dreisler and J. Providencia, Plenum, New York, 1985.

[4] M.Foley and P.A.Madden, Phys. Rev. B 53 (1996) 10589.

[5] W.Kohn and L.J.Sham, Phys. Rev. 140 (1956) A1133.

[6] E.Fermi, Z. Phys. 48 (1928) 73.

[7] P.A.M.Dirac, Proc. Camb. Phil. Soc. 26 (1930) 376.

[8] R.G.Parr and W.Yang, Density-functional Theory of Atoms and Molecules, OUP, Oxford, 1989.

[9] E.H.Lieb, Rev. Mod. Phys. 53 (1981) 603.

[10] D.M.Ceperley and B.J.Alder, Phys. Rev. Lett. 45 (1980) 566.

[11] J.P.Perdew and A.Zunger, Phys. Rev. B 23 (1981) 5048.

[12] U. von Barth and L.Hedin, J. Phys. C 5 (1972) 1629.

[13] S.H.Vosko, L.Wilk and M.Nusair, Can. J. Phys. 58 (1980) 1200.

[14] R.M.Dreizler and E.K.U.Gross, Density Functional Theory, Springer Verlag, Berlin, 1990.

[15] Y.Yang, J.P.Perdew, J.A.Cevary, L.D.McDonald and S.H.Vosko, Phys. Rev. A 41 (1990) 78.

[16] J.P.Perdew and Y.Wang, Phys. Rev. B 33 (1986) 8800.

[17] J.P.Perdew, in Electronic Structure of Solids 91, Ed. P.Ziesche and H.Eschrig Academic Verlay, Berlin, 1991.

[18] D.C.Langreth, M.J.Mehl, Phys. Rev. B, 28 (1983) 1809.

[19] A.D.Becke, Phys. Rev. A 38 (1988) 3098.

[20] C.Lee, W.Yang, R.G.Parr, Phys. Rev. B 37 (1988) 785.

[21] J.P.Perdew, K.Burke, M.Ernzerhof, Phys. Rev. Lett. 77 (1996) 3865.

[22] V.Tschinke, T.Zieglar, Can. J. Chem. 67 (1989) 460.

[23] R.Neumann, N.C.Handy, Chem. Phys. Lett. 266 (1997) 16.

[24] J.P.Perdew, S.Kurth, A.Zupan and P.Blaha, Phys. Rev. Lett. 82 (1999) 2544.

[25] O.Gunnarsson and B.I.Lundqvist, Phys. Rev. B 13 (1976) 4274.

[26] A.D.Becke, J. Chem. Phys. 98 (1993) 1372.

[27] A.D.Becke, J. Chem. Phys., 88 (1988) 1053.

[28] J.P.Perdew and Y.Wang, Phys. Rev. B 45 (1992) 13244.

[29] C.Lee, W.Yang and R.G.Parr, Phys. Rev. B 37 (1988) 785.

CHAPTER 3

RESULTS & DISCUSSION

3.1 Introduction

This chapter is devoted to the most important results of ab initio calculations performed on $Mg_{1-x}Fe_xO$ alloys. In the first section computation details are presented. The structural properties are then depicted in section 2. Section 3 consists of optoelectronic properties while elastic properties are summarized in section 4.

3.2 Computation details

Our calculations are performed using the full-potential linear augmented plane wave (FP-LAPW) method within the framework of the Density functional Theory (DFT) [1]. We use the LDA as parameterized by Perdew and Wang [2], GGA as parameterized by Perdew et al. [3] and WC-GGA [4] for the exchange and correlation potential for the structural properties. As for the electronic properties calculations, the mBj-GGA [5] approximation is used. In the FP-LAPW method, the wavefunction and potential are expanded in spherical harmonic functions inside non-overlapping spheres surrounding the atomic sites (muffin-tin (MT) spheres) and a plane wave basis set in the remaining space of the unit cell (interstitial region) is used. A plane wave cut-off of kmax = $7/RMT$ (where RMT is the smallest MT radius in the unit cell) was used. The MT radius were chosen to be 1.85 au for Fe and 1.8 au for both Mg and O. Meshes of 47 special k-points were chosen in the whole Brillouin zone for for each concentration x of the $\mathrm{Mg}_{1-x}\mathrm{Fe}_x\mathrm{O}$ alloys. The k integration over the Brillouin zone was performed using Monkhorst and Pack, a grid of 10 × 10 × 10 was adopted [6,7]. Both the plane wave cut-off and the number of k-points were varied to ensure total-energy convergence. The iteration process is repeated until the calculated total energy of the crystal converges to less than 0.1 mRyd.

3.3 Structural properties

The structural properties in the strain-free case are obtained by a minimization of the total energy depending on the volume for each composition x in the range $0-1$ (see Figs 3.1, 3.2, 3.3, 3.4 and 3.5). We compute the lattice constants, bulk modulus and the pressure derivative of the bulk modulus by fitting the total energy versus volume according to the Murnaghan's equation of state [8]. The total energy against volume curves for rocksalt phase of MgO one of the parent compounds being studied here are plotted in Figs 3.1, 3.2, 3.3, 3.4 and 3.5 using LDA, GGA and WC-GGA approximation. Note that the rocksalt phase is the more stable state. This is proofed both computationally [9] and experimentally [10].

The lattice constant a_0, bulk modulus B_0 and pressure derivative of the bulk modulus B_0', all at zero pressure, were computed from the curves displayed in figures 3.1, 3.2, 3.3, 3.4, 3.5 by fitting to the Murnaghan's equation of state in an appropriate energy range. A summary of these structural parameters for the rocksalt MgO is listed in Table 3.1. Also shown for comparison are the available experimental and theoretical data for the rocksalt phase. The deviation of a_0 from experiment is smaller than 2%. The agreement of B_0 with experiment is better than 9% whereas that of $B'_0$is within 2%. In fact, our calculated a0 for rocksalt MgO is overestimated with respect to the experimental ones reported in [11,12], whereas our obtained B_0 for rocksalt MgO is underestimated with respect to the experimental values quoted in [11,12]. This is not surprising, the results are consistent with the general trend of the GGA approximations [15,16].

In terms of previous theoretical calculations, our result for a_0 is in excellent agreement with those of Tsuchiya and Kawamura [13] and Karki et al [14]. This is not the case for B_0 where our result is smaller than those reported in [13,14]. For B'_0, the agreement between our calculated value and those quoted in [13,14] is better than 6 and 1%, respectively. As for $Mg_{1-x}Fe_xO$ the obtained results are gathered in Table 3.2. Note that for $x = 0$ (MgO) while the use of LDA and GGA approaches in our case overestimates a_0 with respect to experiment [11,12], a good agreement is obtained between our WC-GGA result and experiment (the deviation is less than 1%). Moreover, our WC-GGA result gives better agreement with experiment than the theoretical data previously reported in Refs. [13,14]. One may conclude then that the WC-GGA approach used in the present work is an acceptable approach for calculating a0 of MgO. The same conclusion can be drawn for B for $x = 0$ where the agreement between our B obtained from LDA, GGA and WC-GGA and experiment is within 8% and 4%, respectively. In terms of previous calculations, our B calculated from WC-GGA approach is in better agreement with experiment [11,12] than those reported in Refs. [13,14]. We observe that the addition of a small amount of Fe atoms in the $Mg_{1-x}Fe_xO$ alloy system leads to the increase of B. this may arise from the bond length which becomes shorter when increasing the Fe concentration. The increase of B with increasing the Fe content is an

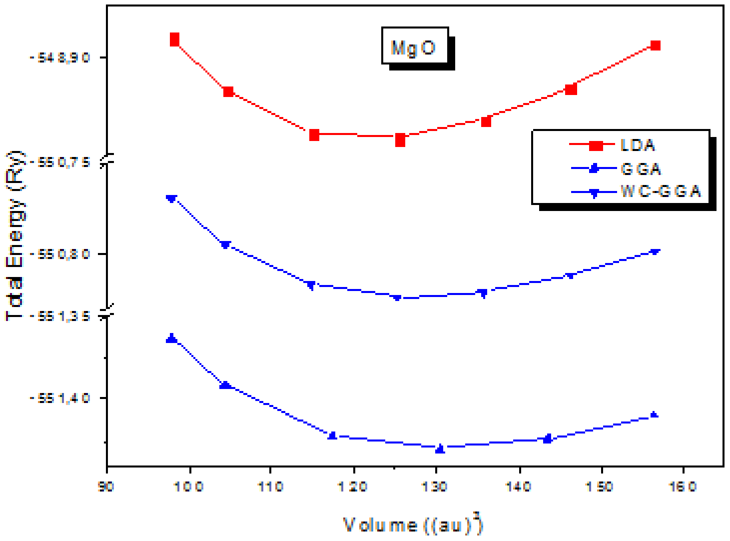

Figure 3.1: a.Total energy vs volume for $Mg_{1-x}Fe_xO$ in B1 phase for composition x=0

indication that $Mg_{1-x}Fe_xO$ becomes less compressible by incorporating more Fe atoms. As far as B' is concerned, our results in all cases (i.e. LDA, GGA and WC-GGA) for MgO are larger than the experimental value quoted in Ref. [12]. Nevertheless, both of the approaches agree well with the B_0 calculated by Gueddim and Bouarissa [9] using the GGA approach. As for FeO, a lattice parameter value of $4.307\AA$ is reported by Rohrer [17]. This is very close to the value of 4.3068 quoted in Ref. [18] for $Fe_{0.946}O$ single crystal. In the absence of data concerning a_0, B and B' for the remaining Fe concentrations, to which we can compare our values, our results are predictions.

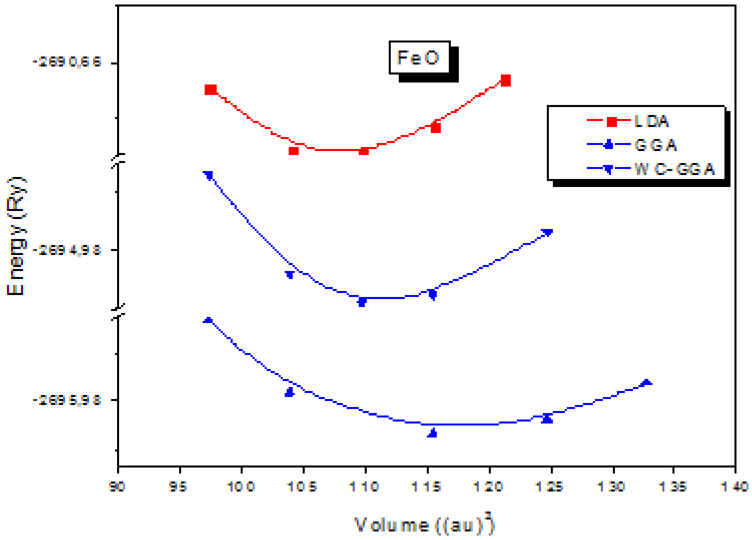

Figure 3.2: b.Total energy vs volume for $Mg_{1-x}Fe_xO$ in B1 phase for composition x=1

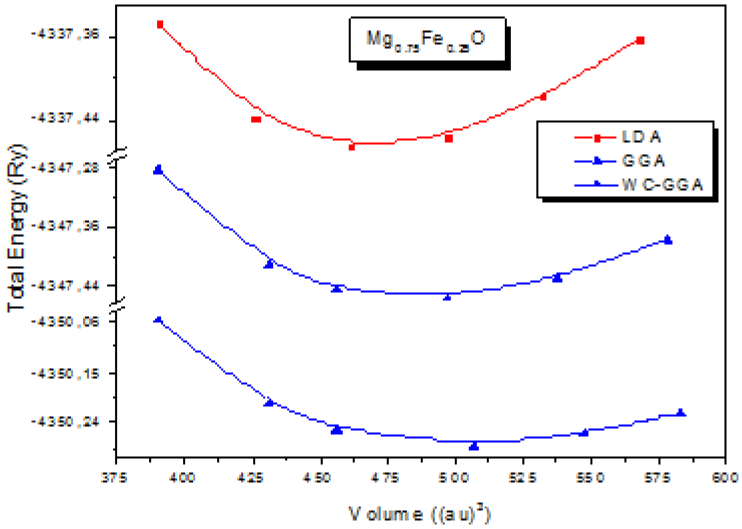

Figure 3.3: c.Total energy vs volume for $Mg_{1-x}Fe_xO$ in B1 phase for composition x=0.25

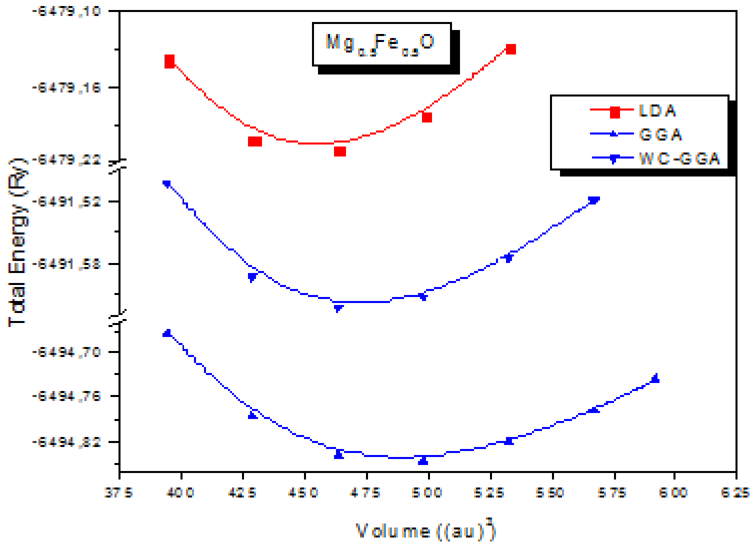

Figure 3.4: d.Total energy vs volume for $Mg_{1-x}Fe_xO$ in B1 phase for composition x=0.5

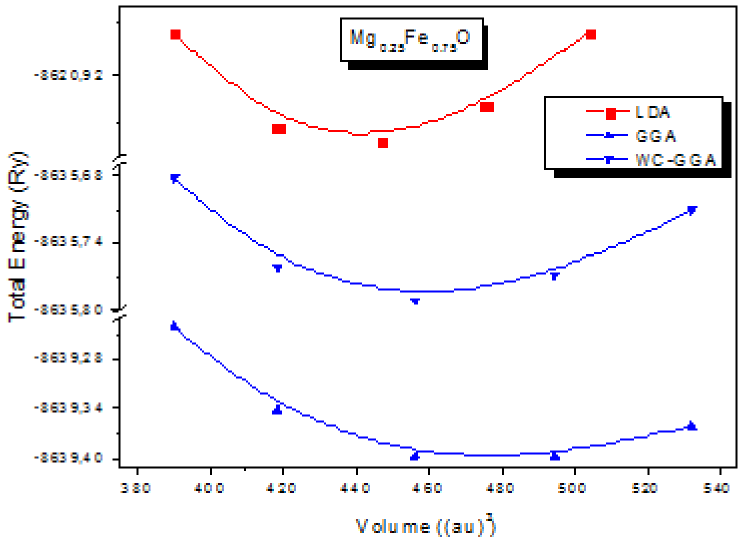

Figure 3.5: e.Total energy vs volume for $Mg_{1-x}Fe_xO$ in B1 phase for composition x=0.75

Table 3.1: Equilibrium lattice constant a0, bulk modulus B0 and pressure derivative of B0 (B')for MgO. aThis work; bExperiment [11]; c Experiment [12]; d Theory [13]; e Theory [14].

	Approximation		
Paramater	LDA	GGA	WC-GGA
a_0	4.164^a	4.259^a	4.221^a ;4.203^b;4.213^c;4.259^d;4.25^e
B_0	170.51^a	147.39^a	154.16 ^{a};160^b;160^c;160^d;159.7^e
B_0'	4.20^a	3.92^a	4.04^a ; 4.15^c;4.01^d;4.26^e

Table 3.2: Equilibrium lattice constant a0, bulk modulus B0 and pressure derivative of B0 (B')for Mg1-xFexO.

	a_0 (Å)			B_0 (GPa)			B_0'		
	LDA	GGA	wc-GGA	LDA	GGA	wc-GGA	LDA	GGA	wc-GGA
0	4.164	4.259	4.221	170.51	147.39	154.16	4.20	3.92	4.04
0.25	4.107	4.203	4.159	199.35	165.06	181.25	4.34	4.45	4.32
0.5	4.061	4.165	4.112	232.88	196.76	212.41	4.40	4.01	4.47
0.75	4.023	4.126	4.073	273.05	220.20	248.38	5.29	4.65	4.84
1	3.992	4.095	4.039	312.22	247.01	283.72	6.56	4.98	5.45

3.4 Optoelectronic properties

3.4.1 **MgO compound**

Figs 3.6 and 3.7 displays the electronic band structure of rocksalt MgO at zero pressure along representative directions of symmetry points ⌈, X and L in the Brillouin zone using both GGA and mBj-GGA approximations. The picture appears to be qualitatively similar to that reported by Gueddim et al. [19] for rocksalt MgO. The zero energy reference is at the top of the valence band which is formed by the triply degenerate hybridized Mg(3p,3s)-O(2p)-like orbitals in an antibonding manner. The bottom of the valence state is a single originating from the bonding Mg(3s)-O(2s) like orbitals that exhibit a weak dispersion. The valence band states always exhibit the behavior to be expected from bonding combinations of hybridized atomic sp3 orbitals. The first conduction band at ⌈ is predominantly of cationic s character. The higher conduction states arise from the hybridization of the Mg(3p,3s)- and O(2p,3s)-like orbitals. We observe that at zero pressure, the maximum of the valence band is at the zone center. The minimum of the conduction band is also at ⌈. Thus, the present results show that at zero pressure, MgO is a direct (⌈−⌈) band gap semiconductor with a fundamental band gap of 7.14 eV (mBj-GGA), 5.63 eV (EV-GGA) and 4.69 (GGA). The density functional calculations of Liu et al. [20] reported a value of 3.72 eV. All values besides that obtained when mBj-GGA is used are underestimated with respect to the experimental result of 7.83 eV [21]. However, one should note that our result reveals better agreement with experiment than that reported by Liu et al. [20]. The underestimation of the band gap is a well-known limitation of both GGA and EV-GGA calculations.

Nevertheless, as far as the energy gap (⌈−⌈) is concerned, EV-GGA gives better results than GGA. It is worth noting that mBj-GGA approximation yields energy gap values (⌈−⌈) very close to the experimental one. This may be expected also for the indirect gaps. Our results as concerning some energy transitions are summarized in Table 3.3.

3.4.2 $\mathbf{Mg_{1-x}Fe_xO}$ alloys

We now turn our attention to the electronic properties, specifically to the energy states of the material system of interest at Fe concentrations of 0%, 25%, 50%, 75% and 100%For that purpose, the optical transition related to the direct (⌈-⌈) and indirect (R-⌈) and (L-⌈) band gaps have been computed using GGA, EV-GGA and mBJ-GGA approaches. Our results are given in Table 3.3. Also shown for comparison are the experimental data which are only available for MgO to the best of our knowledge. Note that the use of both GGA and EV-GGA approaches underestimates energy band-gap Eg(⌈−⌈) with respect to experiment bearing in mind that using EV-GGA approximation results in better accord with experimental findings as for direct band gap energy than do GGA approximation. However, by using mBJ-GGA approach, the values of the direct (⌈−⌈) band gap have been remarkably much improved with respect to experiment [21]. From a fundamental point of view this can be also expected/extrapolated as for the other gaps especially indirect (G-X), (G-L) and (L-G). Thus, using mBj-GGA approach, the electronic band structure and optical properties of $Mg_{1-x}Fe_xO$ at various Fe concentrations have been computed. The quantities of interest are also computed with EV-GGA and GGA approximations for each Fe composition for comparison. Figs 3.6 - 3.15 displays the band structure diagram along selected high-symmetry directions

Table 3.3: Band gap and some transitions energies for Mg1-xFexO.

Composition %	GGA	EV-GGA	mBj	Other calc	Experiment
0 (⌈-⌈)	4.69	5.63	7.14	5.25 [19]	7.83[21]
				3.72 [20]	
25(R-⌈) spin up	1.02	1.90	3.43		
50(R-⌈) spin up	0.88	1.80	3.20		
75(R-⌈) spin up	0.80	1.58	2.87		
1(L-⌈) spin up	0.83	1.62	3.04		2 [17]

of the Brillouin zone of $Mg_{1-x}Fe_xO$ for various Fe compositions in the range 0-1 using mBj-GGA approach. For the latter, the spin direction (↑ and ↓) is taken as the direction of Fe spin (majority spin ↑ direction) as shown in Figs 3.8, 3.10, 3.12 and 3.14 and (minority spin ↓ direction) as displayed in Figs 3.9, 3.11, 3.13 and 3.15. Equilibrium lattice parameters are used so as to compute the spin-dependent polarized electronic band structure of ferromagnetic rocksalt $Mg_{1-x}Fe_xO$. For MgO (Figs 3.6 and 3.7), the overall features of these bands are similar as reported in Refs; [19,20]. The conduction bands seem to be more dispersive than the valence bands. This could be traced back to the fact that the conduction bands are more delocalized than the valence ones. As regards $Mg_{1-x}Fe_xO$ (Figs 3.6 - 3.15), one can note that the introduction of Fe to MgO (hybridization of Fe 3d and O 2p orbitals) has resulted in a spin-split valence band. which makes the material half-metallic with the majority spin band being higher. The Fermi level is in the conduction for spin down calculations, indicating a degenerate n-type material.

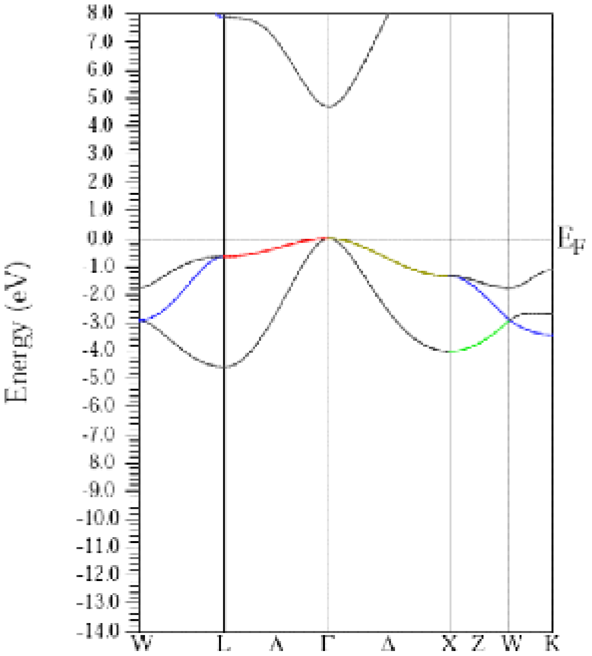

Figure 3.6: a. Electron band struture using : GGa approximation (MgO)

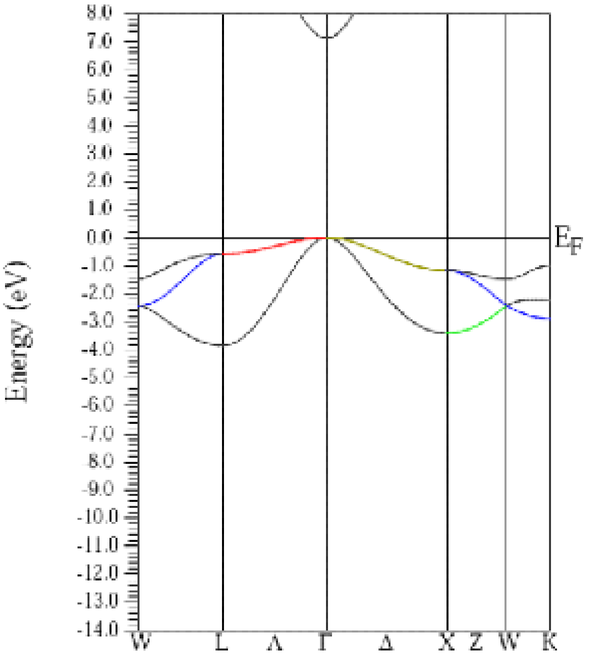

Figure 3.7: b. Electron band structure using : mBj approximation (MgO)

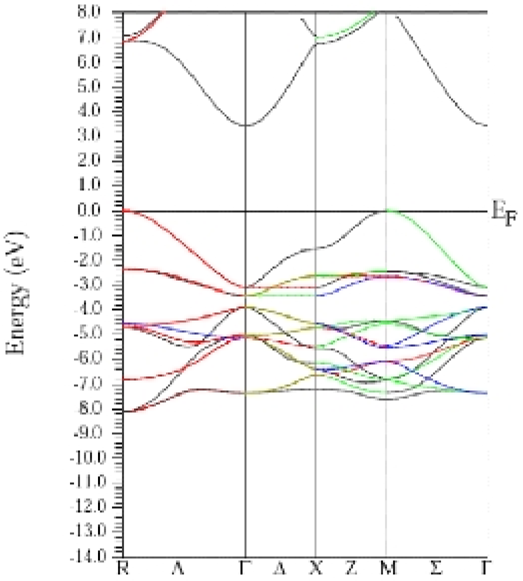

Figure 3.8: a. Electron band structure for $Mg_{1-x}Fe_xO$ in B1 phase for composition x=0.25, using mBj-GGa approximation for spin up

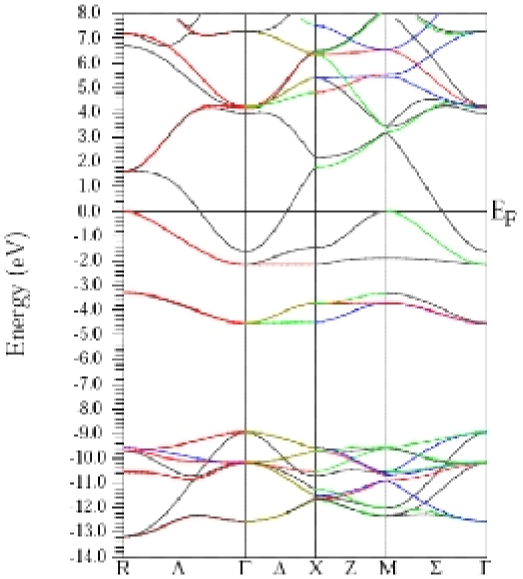

Figure 3.9: b. Electron band structure for $Mg_{1-x}Fe_xO$ in B1 phase for composition x=0.25, using mBj-GGa approximation for spin down

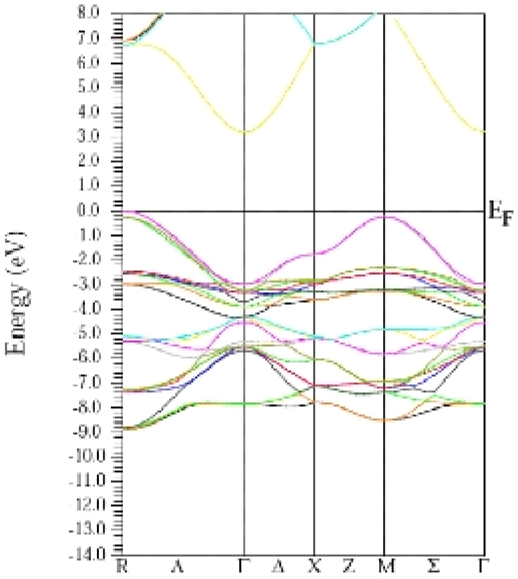

Figure 3.10: c. Electron band structure for $Mg_{1-x}Fe_xO$ in B1 phase for composition x=0.5 using mBj-GGa approximation for spin up

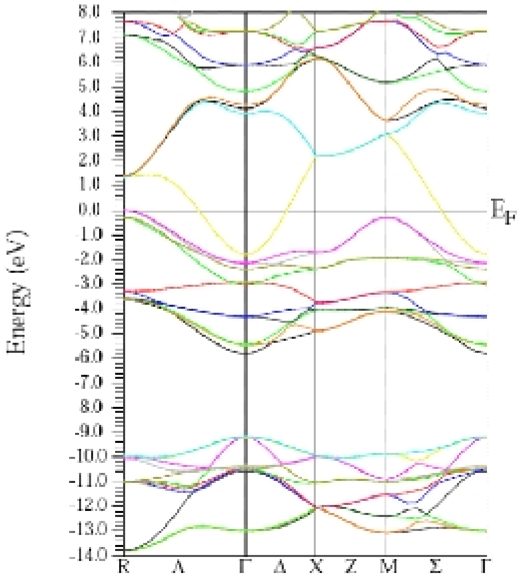

Figure 3.11: d. Electron band structure for $Mg_{1-x}Fe_xO$ in B1 phase for composition x=0.5, using mBj-GGa approximation for spin down.

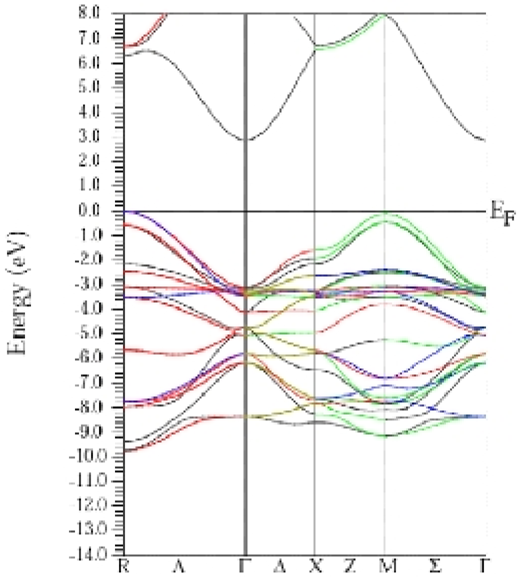

Figure 3.12: e. Electron band structure for $Mg_{1-x}Fe_xO$ in B1 phase for composition $x = 0.75$ using mBj-GGa approximation for spin up.

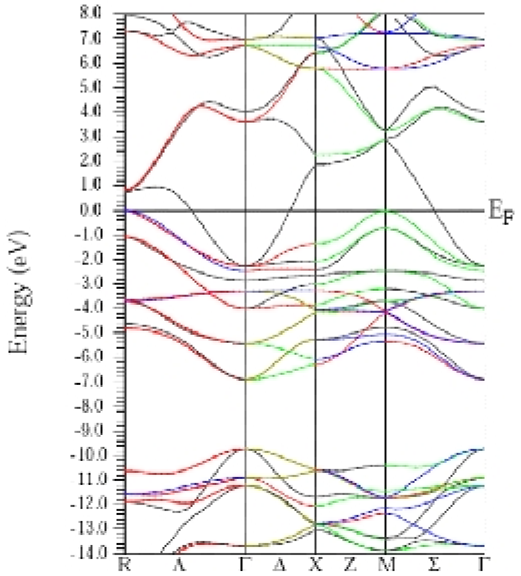

Figure 3.13: f. Electron band structure for $Mg_{1-x}Fe_xO$ in B1 phase for composition $x = 0.75$using mBj-GGa approximation for spin down.

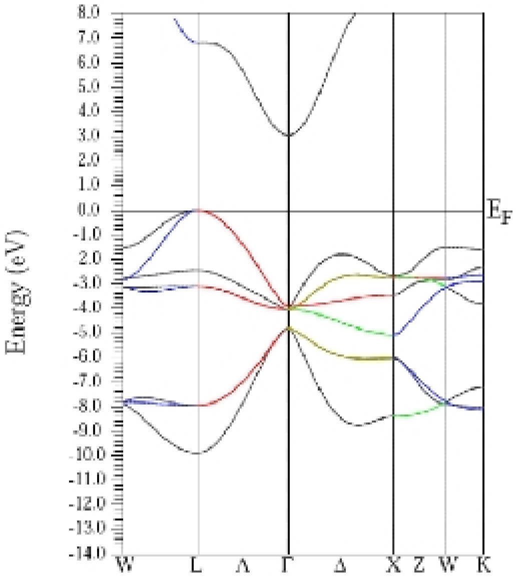

Figure 3.14: g. Electron band structure for $Mg_{1-x}Fe_xO$ in B1 phase for composition $x = 1$ using mBj-GGa approximation for spin up.

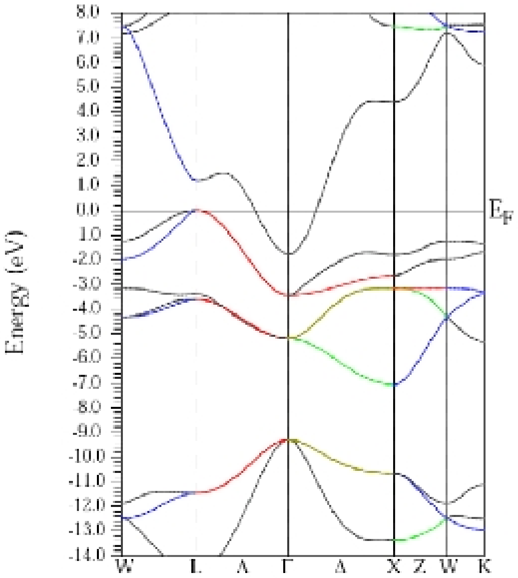

Figure 3.15: h. Electron band structure for $Mg_{1-x}Fe_xO$ in B1 phase for composition $x = 1$ in B1 phase using mBj-GGa approximation for spin down.

3.5 Optical properties

The optical properties of semiconducting materials are strongly related to the electronic band structure. In this respect, the optical response function, that is, real ε_1(E) and imaginary ε_2(E) parts of the dielectric function, for $Mg_{1-x}Fe_xO$ with Fe composition in the range 0-1, where E is the photon energy, are plotted in Figs. 3.16 and 3.17, respectively. ε_2(E) was been obtained directly from the electronic band structure calculation, using the expression,

$$\varepsilon_2(\omega) = \frac{e^2 h}{2m^2\omega^2} \sum_{V,C} \int_{BZ} \left| M_{CV}\left(k\right)^2 \right| \delta\left[\omega_{CV}\left(k\right) - \omega\right] d^3k \tag{3.1}$$

where M_{CV}(k) are the transition moments elements. The integral was made over the first Brillouin zone, the dipole moments : M_{CV}(k) $= \langle U_{CK} \left| e.\nabla \right| U_{VK} \rangle$, where e is the polarization vector of the electric field, are matrix elements for direct transitions between valence U_{VK} and conduction-band U_{CK} states, and $\bar{h}\omega_{Cv}(k) = \omega_{CV} - \omega_{VK}$ is the excitation energy. The real part of $\varepsilon(\omega)$ is derived from the imaginary part using the Kramers–Kronig relations,

$$\varepsilon_1\left(\omega\right) = 1 + \frac{2}{\pi} P \int_0^\infty \frac{\omega' \varepsilon_2\left(\omega'\right)}{\omega'^2 - \omega^2} d\omega' \tag{3.2}$$

where P implies the principal value of the integral.

From an inspection of Figs. 3.16 and 3.17, we observe that the behavior of ε_1(E) and ε_2(E) parts is rather similar for the various Fe concentrations being considered in the present work with some differences in details. Note that the main peak of the real part for MgO occurs at around E $\approx$ 11 eV (Fig. 3.16). As far as the Fe content becomes larger the peak is shifted towards different energies. We see that the position and broadening of the critical peaks varies as a function of Fe concentrations. The amplitude of the peaks seems to be random. Besides, the shape is that expected for a harmonic oscillator with a resonant frequency at about 14 eV. The resonant frequency is shifted towards higher energies as the Fe concentration in $Mg_{1-x}Fe_xO$ material system is increased. Focusing on $\varepsilon_2(E)$, the critical points of MgO are observable in the graph of Fig. 3.17. It is found that the fundamental band gap (E_0) is significantly broadened in $Mg_{1-x}Fe_xO$. We note that this effect can be seen in both $\varepsilon_1(E)$ and $\varepsilon_2(E)$. The origin of this broadening might be explained as a result of a relaxation of the requirement of momentum conservation. This relaxation is due to the presence of impurities that provide additional scattering mechanisms. This band gap broadening is aided by a transfer of spectral weight from higher energies to lower ones. Beyond this point, the curves increase rapidly. This is due to the fact that the number of points contributing towards $\varepsilon_2(E)$ increases abruptly. Similar behavior has been reported by Bouarissa for InP [22].

3.6 Elastic properties

The elastic properties play a major role in providing valuable information about the binding characteristic between adjacent atomic planes, anisotropic character of binding and structural stability [15]. Furthermore, knowledge of elastic constants is needed to control strain and relaxation in heterostructures [23]. For this purpose, the elastic properties of the material under investigation in B1 structure have been calculated at zero and under hydrostatic pressure using the method developed by Charpin [15,24].

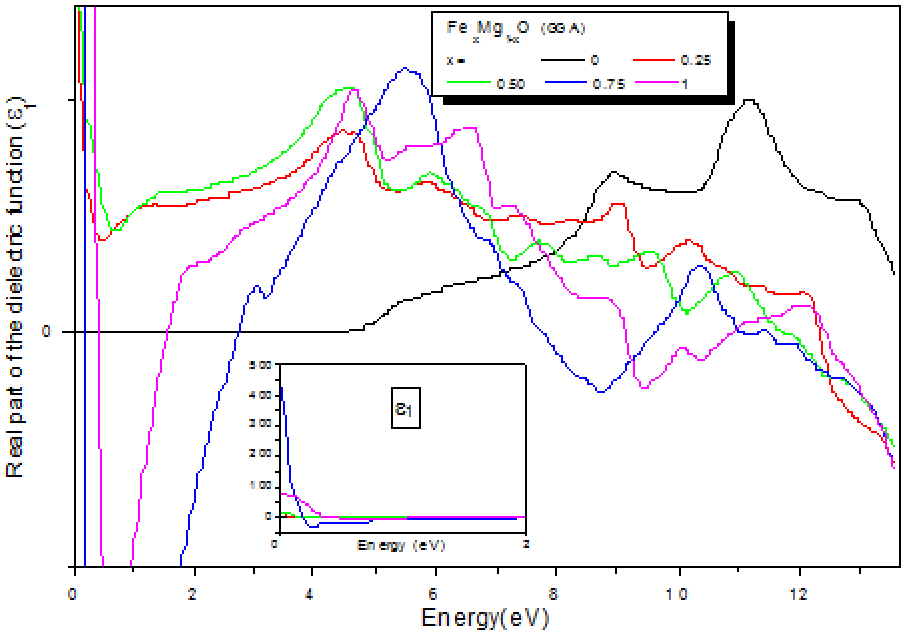

Figure 3.16: Real part of the dielectric function for $Mg_{1-x}Fe_xO$ in B1 phase for compisition a. x=0, b. x=0.25, c. x=0.5, d. x=0.75 and e. x=1 using mBj-GGa approximation.

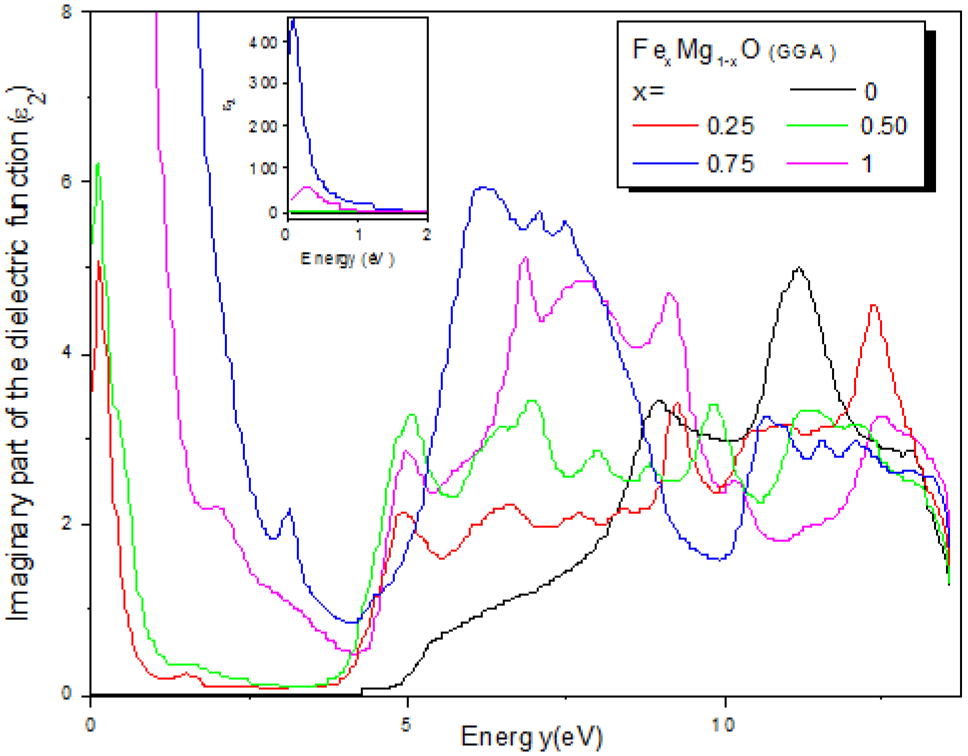

Figure 3.17: Imaginary part of the dielectric function for $Mg_{1-x}Fe_xO$ in B1 phase for compisition a. x=0, b. x=0.25, c. x=0.5, d. x=0.75 and e. x=1 using mBj-GGa approximation.

It is well known that a cubic crystal has only three independent elastic constants, namely C_{11}, C_{12}, and C_{44}. Hence a set of three equations is needed to determine the constants [25]. The first equation involves calculating the bulk modulus (B), which is related to the elastic constants by [26],

$$B = \frac{1}{3}\left(C_{11} + 2C_{12}\right) \tag{3.3}$$

The second equation involves performing volume conservative tetragonal strain tensor δ.

$$\overrightarrow{\delta} = \begin{pmatrix} \delta & 0 & 0 \\ 0 & \delta & 0 \\ 0 & 0 & \frac{1}{1+\delta^2} - 1 \end{pmatrix} \tag{3.4}$$

The application of this strain has an effect on the total energy from its unstrained value as follows,

$$E\left(\delta\right) = \left(C_{11} - C_{12}\right) 6V_0\delta^2 + O\left(\delta^2\right) \tag{3.5}$$

Where V_0 is the volume of the unit cell. Finally, for the last type of deformation, we used the volume-conserving rhombohedral strain tensor given by,

$$\overrightarrow{\delta} = \frac{\delta}{3}\begin{pmatrix} 1 & 1 & 1 \\ 1 & 1 & 1 \\ 1 & 1 & 1 \end{pmatrix} \tag{3.6}$$

Which transform the total energy to,

$$E(\delta) = \frac{V_0}{3}(C_{11} + 2C_{12} + 4C_{44})\,\delta^2 + O\left(\delta^2\right) \tag{3.7}$$

These three equations form the set of equations needed to determine the full elastic tensor.

For the cubic structure there are three independent coefficients: C_{11}, C_{12}, and C_{44}. Our results concerning these elastic constants are listed in Table 3.4. It constrast to the general trend that the LDA approach overpredicts the elastic constants and GGA approach improve on the chemical bonding and elastic constants of materials [16,27], our calculated elastic constants present a violation of this trend as shown in Figs 3.18, 3.19 and 3.20. As for the WC-GGA, the calculated quantities are generally lying between those obtained with LDA and GGA. It is worth noting that C_{11} coefficients (compression/stretching) are much higher than C_{44} ones (shear) for both LDA and GGA approaches. This suggests that B1 structure is less resistant to the applied shear.

The bulk modulus (B_0) which is related to the elastic constants can also be obtained by,

$$B_0 = \frac{1}{3}(C_{11} + 2C_{12}) \tag{3.8}$$

Using Eq. (3.8), the B_0 has been calculated for LDA, GGA and WC-GGA approaches. Our results are presented in Table 3.2 showing a very good agreement with those quoted in Table 3.1. A given crystal structure cannot exist in a stable or metastable phase unless its elastic constants obey certain relationships. The traditional mechanical stability conditions in cubic crystals on the elastic constants are known as

Table 3.4: Elastic Constants C11, C12 and C44 for Mg1-xFexO

	C_{11}			C_{12}			C_{44}		
	GGA	LDA	wc-GGA	GGA	LDA	wc-GGA	GGA	LDA	wc-GGA
0	341.52	314.03	329.70	80.68	64.64	72.63	146.90	151.80	145.58
0.25	360.39	318.72	356.59	108.94	101.62	101.00	128.73	143.65	138.04
0.5	440.58	339.42	390.62	120.72	126.53	125.85	86.91	82.86	81.10
0.75	514.04	448.23	481.02	136.34	116.37	130.49	31.75	12.86	21.56
1	484.81	315.66	405.89	197.88	221.13	209.75	-60.28	-79.49	-75.62

[33,34],

$$C_{11} - C_{12} \succ 0, C_{44} \succ 0, and C_{11} + 2C_{12} \succ 0 \tag{3.9}$$

We point out that the above criteria are fulfilled for $Mg_{1-x}Fe_xO$ with the B1 phase at zero pressure except for composition $x = 0$. This reflects the mechanical stability of the $Mg_{1-x}Fe_xO$ in the NaCl-type at normal conditions except for FeO. This could be traced back to the fact that FeO is stochoimetric $Fe_{0.946}O$ [17,18].

Elastic Constants C_{11}, C_{12} and C_{44} for $Mg_{1-x}Fe_xO$.

3.7 Conclusion

Structural, electronic, optical and elastic properties of $Mg_{1-x}Fe_xO$ alloys have been theoretically investigated using ab initio calculations in the frame work of density functional theory with several exchange-correlation approximations (LDA, GGA, EV-GGA,

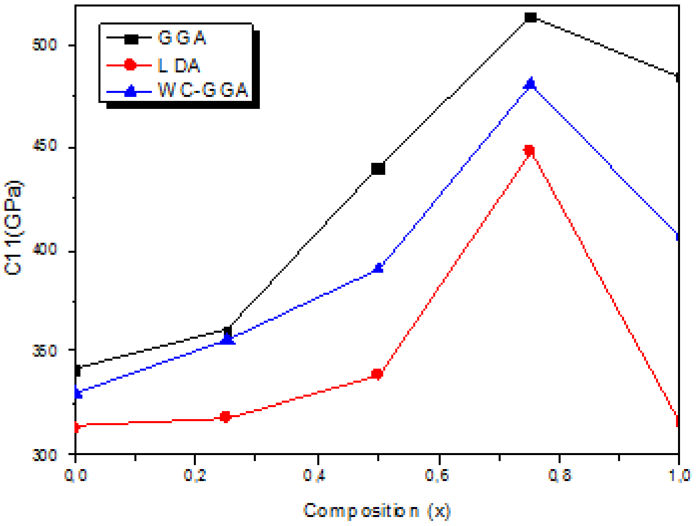

Figure 3.18: C_{11} elastic constant for $Mg_{1-x}Fe_xO$ in B1 phase for composition a. x=0, b. x=0.25, c. x=0.5, d. x=0.75 and e. x=1 using LDA, GGa and mBj-GGa approximation.

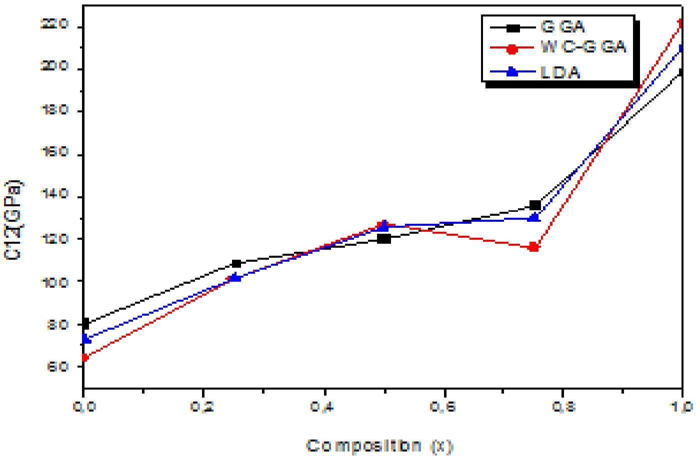

Figure 3.19: C_{12} elastic constant for $Mg_{1-x}Fe^xO$ in B1 phase for composition a. x=0, b. x=0.25, c. x=0.5, d. x=0.75 and e. x=1 using LDA, GGa and mBj-GGa approximation.

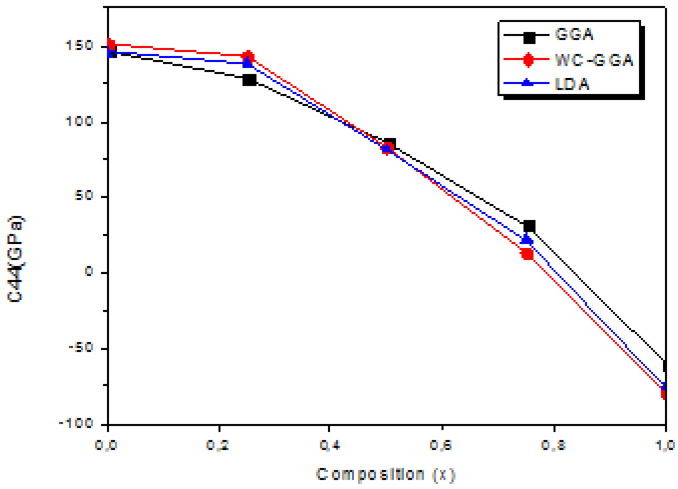

Figure 3.20: C_{44}elastic constant for $Mg_{1-x}Fe_xO$ in B1 phase for compisition a. x=0, b. x=0.25, c. x=0.5, d. x=0.75 and e. x=1 using LDA, GGa and mBj-GGa approximation.

WC-GGA and mBj-GGA). The obtained results for MgO are in satisfactory accordance with the available data. As for $Mg_{1-x}Fe_xO$ alloys, our results are predictions and may serve as a reference regarding the lack on information on this system.

BIBLIOGRAPHY

[1] P. Hohenberg, W. Kohn, Inhomogeneous electron gas, Phys. Rev. 136 (1964) B864–B871.

[2] J.P. Perdew, Y. Wang, Phys. Rev. B 45 (1992) 13244.

[3] J.P. Perdew, S. Burke, M. Ernzerhof, Phys. Rev. Lett. 77 (1996) 3865.

[4] Z. Wu, R.E. Cohen, Phys. Rev. B 73 (2006) 235116.

[5] F. Tran, P. Blaha, Phys. Rev. Lett. 102 (2009) 226401.

[6] H.J. Monkhorst, J.D. Pack, Special points for Brillouin-zone integrations, Phys. Rev. B 13 (1976) 5188–5192.

[7] J.D. Pack, H.J. Monkhorst, Special points for Brillouin-zone integrations – a reply, Phys. Rev. B 16 (1977) 1748–1749.

[8] F.D. Murnaghan, Proc. Natl. Acad. Sci. USA 30, 244 (1944).

[9] A.Gueddim, N.Bouarissa, A.Villesuzanne, Phys. Scr. 80 (2009) 055702

[10] T.S.Duffy, R.J.Hemley and H-K.Mao, Phys. Rev. Lett.74 (1995) 1371

[11] S.Adachi, Properties of Group IV, III-V and II-VI Semiconductors, Chichester: Wiley, 2005.

[12] Y.Fei, Am. Mineral. 84 (1999) 272.

[13] T.Tsuchiya and K.Kawamura, J. Chem. Phys. 114 (2001) 10086

[14] B.B.Karki, L.Stixrude, S.J.Clark, M.C.WarrenC, G.J.Ackland and J.Crain, Am. Mineral. 82 (1997) 51.

[15] A.Gueddim, N.Fakroun, N.Bouarissa, A.Villesuzanne, Mater. Chem. Phys. 118 (2009) 427

[16] J.Wróbel and J.Piechota, Solid State Commun. 146 (2008) 324.

[17] G.S.Rohrer, Structure and Bonding in Crystalline Materials, Cambridge Univ. Press, UK, 2004.

[18] S.D.Jacobson et al., J. Geophysical Research, vol.107 n°B2 (2002) 10029.

[19] A.Gueddim, N.Bouarissa, A.Villesuzanne, Optik 124 (2013) 2670.

[20] Z.-J. Liu, Y.-X. Du, X.-L. Zhang, J.-H. Qi, L.-N. Tian, Y. Guo, Density functional calculations of the electronic structure and optical properties of magnesium oxide, Phys. Status Solidi B 247 (2010) 157–162.

[21] R.C. Whited, C.J. Flaten, W.C. Walker, Exciton thermoreflectance of MgO and CaO, Solid State Commun. 13 (1973) 1903–1905.

[22] N. Bouarissa, Solid-State Electron. 44 (2000) 2193.

[23] A. Gueddim, N. Bouarissa, Appl. Surf. Sci. 253 (2007) 7336.

[24] A.Gueddim, N.Bouarissa, A.Villesuzanne, Comput. Mater. Sci. 48 (2010) 490.

[25] S. Saib, N. Bouarissa, Solid State Eletcron. 50 (2006) 763.

[26] E. Schreiber, O.L. Anderson, N. Soga, Elastic Constants and their Measurements, McGraw-Hill, New York, 1973.

[27] S. Saib, N. Bouarissa, Phys. Status Solidi (b) 244 (2007) 1063.

Conclusion

The physical properties such as the structural, electronic, optical and elastic features of $\mathrm{Mg}_{1-x}\mathrm{Fe}_x\mathrm{O}$ alloys have been determined via first principles calculations performed within density functional theory. In dealin with electron-electron interaction, the exchange-correlation effects are treated using LDA, GGA and WC-GGA approximations as concerns the structural and elastic properties whereas GGA, EVGGA and mBj-GGA approaches are employed when calculating the electronic and optical properties. The major obtained results can be drawn as follows:

Structural properties

The structural properties in the strain-free case are obtained by a minimization of the total energy depending on the volume for each composition x in the range $0-1$. We compute the lattice constants, bulk modulus and the pressure derivative of the bulk modulus by fitting the total energy versus volume according to the Murnaghan's equation of state. It is noted that for$x = 0$ (MgO) while the use of LDA and GGA approaches in our case overestimates a_0 with respect to experiment, a good agreement is obtained between our WC-GGA result and experiment (the deviation is less than 1%). Moreover, our WC-GGA result gives better agreement with experiment than the previous theoretical data. One may conclude then that the WC-GGA approach used in the present work is an acceptable approach for calculating a0 of MgO. The same conclusion can be drawn for B for $x = 0$ where the agreement between our B obtained from LDA, GGA and WC-GGA and experiment is within 8% and 4%, respectively. In terms of previous calculations, our B calculated from WC-GGA approach is in better agreement with experiment. We observe that the addition of a small amount of Fe atoms in the $\mathrm{Mg}_{1-x}\mathrm{Fe}_x\mathrm{O}$ alloy system leads to the increase of B. This may arise from the bond length which becomes shorter when increasing the Fe concentration. The increase of B with increasing the Fe content is an indication that $\mathrm{Mg}_{1-x}\mathrm{Fe}_x\mathrm{O}$ becomes less compressible by incorporating more Fe atoms. As far as B' is concerned, our results in all cases (i.e. LDA, GGA and WC-GGA) for MgO are larger than the experimental value quoted in Ref. [12]. As for FeO, a lattice parameter value of 4.039 is found. This compares well with the other reported values.In the absence of data concerning a_0, B and B' for the remaining Fe concentrations, to which we can compare our values, our results are predictions.

Optoelectronic properties

The energy states of the material system of interest at Fe concentrations of 0%, 25%, 50%, 75% and 100% are examined. The optical transition related to the direct (⌈-⌈) and indirect (R-⌈) and (L-⌈) band gaps have been computed using GGA, EV-GGA and mBj-GGA approaches. We note that the use of both GGA and EV-GGA approaches underestimates energy band-gap $\mathrm{E}_{\lceil}^{\lceil}(\lceil-\lceil)$ with respect to experiment bearing in mind that using EV-GGA approximation results in better accord with experimental findings as for direct band gap energy thant do GGA approximation. However, by using mBJ-GGA approach, the values of the direct (⌈−⌈) band gap have been remarkably much improved with respect to experiment.

Optical properties

The optical properties of semiconducting materials are strongly related to the electronic band structure. In this respect, the optical response function, that is, real $\varepsilon_1(E)$ and imaginary $\varepsilon_2(E)$ parts of the dielectric function, for $\mathrm{Mg}_{1-x}\mathrm{Fe}_x\mathrm{O}$ with Fe composition in the range 0-1, are calculated from the electronic band structure calculation.

The real part of $\varepsilon(\omega)$ is derived from the imaginary part using the Kramers–Kronig relations. The behavior of $\varepsilon_1(E)$ and $\varepsilon_2(E)$ parts is rather similar for the various Fe concentrations with some differences in details. Note that the main peak of the real part for MgO occurs at around $E \approx 11eV$ (Fig. 3.3). As far as the Fe content becomes larger the peak is shifted towards different energies. The amplitude of the peaks seems to be random. Besides, the shape is that expected for a harmonic oscillator with a resonant frequency at about 14 eV. The resonant frequency is shifted towards higher energies as the Fe concentration in $\mathrm{Mg}_{1-x}\mathrm{Fe}_x\mathrm{O}$ material system is increased. Focusing on $\varepsilon_2(E)$, the critical points of MgO are observable in the graph of Fig. 3.4. It is found that the fundamental band gap (E_0) is significantly broadened in $\mathrm{Mg}_{1-x}\mathrm{Fe}_x\mathrm{O}$. We note that this effect can be seen in both $\varepsilon_1(E)$ and . The origin of this broadening might be explained as a result of a relaxation of the requirement of momentum conservation. This relaxation is due to the presence of impurities that provide additional scattering mechanisms.

Elastic properties

The elastic properties of the material under investigation in B1 structure have been calculated at zero and under hydrostatic pressure using the method developed by Charpin.For the cubic structure there are three independent coefficients: C_{11}, C_{12}, and C_{44}. It constrast to the general trend that the LDA approach overpredicts the elastic constants and GGA approach improve on the chemical bonding and elastic constants of materials, our calculated elastic constants present a violation of this trend. As for the WC-GGA, the calculated quantities are generally lying between those obtained with LDA and GGA. It is worth noting that C_{11} coefficients (compression/stretching) are much higher than C_{44} ones (shear) for both LDA and GGA approaches. This suggests that B1 structure is less resistant to the applied shear.

We point out that the stability criteria are fulfilled for $Mg_{1-x}Fe_xO$ with the B1 phase at zero pressure except for composition $x = 0$. This reflects the mechanical stability of our alloys at normal conditions except for FeO. This could be traced back to the fact that FeO is stochoimetric $Fe_{0.946}O$ [17,18]. The obtained results for MgO are in satisfactory accordance with the available data. As for $Mg_{1-x}Fe_xO$ alloys, our results are predictions and may serve as a reference regarding the lack on information on this system.